

Wave energetics of the southern hemisphere of Mars

Michael Battalio*, Istvan Szunyogh, Mark Lemmon

Department of Atmospheric Science, Texas A & M University, United States

ARTICLE INFO

Article history:

Received 31 July 2017

Revised 9 March 2018

Accepted 12 March 2018

Available online 13 March 2018

Keywords:

Atmospheres

dynamics

Mars

atmosphere

Mars

climate

ABSTRACT

An assessment of the energetics of transient waves in the southern hemisphere of Mars is presented using the Mars Analysis Correction Data Assimilation (MACDA) dataset (v1.0) and the eddy kinetic energy equation. The dataset is divided into four representative periods covering the summer and winter solstices, a late fall period, and an early spring period for three Mars years. Spring eddies are the most intense, with eddies during the fall being less intense due to a marginally more stable mean-temperature profile and reduced recirculation of ageostrophic geopotential fluxes compared to the spring. Eddy kinetic energy during winter is reduced in intensity as a result of the winter solstitial pause in wave activity, and eddy kinetic energy during the summer is limited. Baroclinic energy conversion acts as a source in fall and spring but disappears during the winter as a result of a stabilized vertical temperature profile. Barotropic energy conversion acts as both a source and a sink of eddy kinetic energy, being most positive during the solstitial pause. Eddies take a northwest to southeast track across the southern highlands in the fall but have a more zonal track in the spring due to stronger eddy kinetic energy advection. Wave energetics is less intense in the southern compared to the northern hemisphere as a result of a shallower baroclinically unstable vertical profile.

© 2018 Elsevier Inc. All rights reserved.

1. Introduction

Transient waves in the atmosphere of Mars have been a subject of study for several decades. Waves in the northern hemisphere have been more extensively investigated (e.g., Banfield et al., 2004; Kuroda et al., 2007; Kavulich et al., 2013; Wang et al., 2013; Wang and Toigo, 2016; Battalio et al., 2016) since they are the more intense and have also been observed from the ground (Barnes, 1980; 1981). However, midlatitude transient waves occur in the southern hemisphere as well (e.g., Hinson and Wilson, 2002).

1.1. Martian southern hemisphere waves

The earliest modeling studies found that transient waves in both hemispheres had a wave number between 2 and 4 (Leovy, 1969) and avoided areas of strong topographical gradients (Blumsack and Gierasch, 1972), though it was not until sometime later that the presence of waves in the southern hemisphere was established. An early modeling investigation (Barnes et al., 1993), found that southern hemisphere waves were present at reduced amplitudes but slightly higher wave numbers (> 3) compared to

the northern hemisphere, and topography seemed to play a role in suppressing eddy activity.

The first observations of transient waves in the southern hemisphere were reported by Hinson and Wilson (2002) using limb retrievals from the Thermal Emission Spectrometer (TES), part of the Mars Global Surveyor. A 2-sol period, wave number 3 disturbance was found to dominate the signal after winter solstice ($L_s = 134^\circ$ – 148°). Additionally, their study [using a general circulation model (GCM)] corroborated this finding, showing that wave amplitude was zonally modulated so the waves had the most energy between 180° and 330°E , suggesting that the waves were baroclinically forced.

A seasonally evolving view of southern hemisphere transient waves was provided by Banfield et al. (2004) using TES nadir retrievals. Wave number 1–3 eddies were present both before and after the winter solstice. Wave number 1 waves in the southern hemisphere were found to be weaker than in the northern hemisphere in general but had indications of a relatively strong wave number 1 component during the initiation of the Mars year (MY) 25 global-scale dust storm (GDS). The wave number 3 component was somewhat weaker than the wave number 1 component, and it was confined to the lowest scale height of the atmosphere. Waves were limited to storm tracks between 190° and 320°E , just to the south of the Tharsis Plateau and near Argyre Planitia and near 60°E , south of Hellas Planitia. Unlike in the northern hemisphere, where GCM simulations have found the areas of maximum

* Corresponding author. Current address: Harvard-Smithsonian Center for Astrophysics MS 50, 60 Garden Street, Cambridge, MA 02138, United States.

E-mail address: michael@battalio.com (M. Battalio).

eddy amplitude to be in the lowland planitias (Hollingsworth and Barnes, 1996), the origin of the southern hemisphere storm tracks was unclear (Banfield et al., 2004).

During the spring, the strongest transient wave from TES observations of the southern hemisphere was found to be wave number 1, with an intensification during global dust events (Imamura and Kobayashi, 2009). These transient waves were weaker than both their northern hemisphere counterparts and the southern hemisphere wave number 1 stationary wave. Imamura and Kobayashi (2009) hypothesized that transient wave number 1 was the strongest due to an inverse energy cascade from wave numbers 2 and 3.

Southern hemisphere transient waves play an important role in the annual dust cycle. In numerical simulations, regional dust storms can form from southern hemisphere transient waves (Basu et al., 2006), and rarely, these storms can develop into a GDS if additional lifting centers across the hemisphere are activated, for example in Argyre Planitia, to the south of the Tharsis Plateau, or from coincident northern hemisphere transient waves (Wang et al., 2003). The MY 25 GDS was activated in this way (Strausberg, 2005), and the MY 28 GDS was also the result of southern hemisphere dust lifting. The model of Basu et al. (2006) indicated that weak residual transient wave activity after the usual spring period contributed to the initiation of GDSs. Regional dust storms in the southern hemisphere were observed to travel zonally between $L_s = 135^\circ$ – 180° , as opposed to the more meridional orientation of northern hemisphere dust storms (Wang et al., 2011; Wang and Richardson, 2015; Guzewich et al., 2015, 2017). Southern hemisphere local dust storms are generally more isolated, of shorter duration (< 5 sols), and smaller in spatial extent than their northern counterparts (Wang et al., 2013; Wang and Richardson, 2015). Frontal, flushing dust storms also propagate from the northern to the southern hemisphere through the channels between Tharsis and Arabia Terra.

Transient waves are important for the deposition of CO_2 onto the polar ice caps. Mars Climate Sounder observations have shown that between 3 and 20 percent of seasonal CO_2 deposits south of 70°S occur because of snowfall and that dynamical cooling as a result of orographic lifting is an order of magnitude stronger than radiative cooling (Hayne et al., 2012, 2014). MGCM simulations by Kuroda et al. (2013) showed that CO_2 ice is deposited by snowfall as a result of cloud formation below 20 km in the cold phase of transient waves in the northern hemisphere. Ultimately, the superposition of transient and stationary waves provides the conditions cold enough for CO_2 supersaturation. Snowfall is therefore modulated longitudinally by the location of the transient wave storm track (Noguchi et al., 2017).

Waves in the southern hemisphere follow a repeatable, yearly pattern of activity (Lewis et al., 2016). During the summer, transient waves are virtually non-existent but slowly increase in amplitude during the fall period, with their preferred latitudes simultaneously moving equatorward. Waves begin during $L_s = 15^\circ$ – 60° , then abruptly cease during $L_s = 70^\circ$ – 110° due to stabilization of the atmosphere by midlevel polar warming (Kuroda et al., 2007; Mulholland et al., 2016). Eddies resume after $L_s = 120^\circ$, and their region of growth returns poleward during the subsequent 50° of areocentric longitude. This latitudinal movement tracks the advance and retreat of the polar ice caps in both hemispheres (see Fig. 2 of Mooring and Wilson, 2015).

1.2. Eddy energetics

Local eddy energetics was established as a diagnostic tool in the terrestrial atmosphere in the 1990s. Orlandi and Katzfey (1991) formalized a local eddy kinetic energy (EKE) budget equation and applied it to terrestrial cyclogenesis. The results of

a series of studies based on the EKE equation (e.g., Chang, 1993; Orlandi and Chang, 1993) revealed a repeating process of development. Eddies grow by converting available potential energy into EKE (baroclinic energy conversion), which propagates downstream to trigger further baroclinic development in regions of enhanced baroclinic instability. Eddies decay upon reaching the downstream edge of the storm track by barotropic conversion of the EKE into the kinetic energy of the zonal mean. Barotropic instabilities can occasionally contribute to eddy growth as well, particularly closer to the subtropics (Ha et al., 2013), with the main sinks of EKE being diabatic energy losses (McLay and Martin, 2002) and frictional dissipation (Chang, 2001; Decker and Martin, 2005; Ahmadi-Givi et al., 2014).

The first application of the eddy energetics of Orlandi and Katzfey (1991) to the atmosphere of Mars was performed for a period just before the northern hemisphere winter solstice, using the GFDL Mars Global Circulation Model (MGCM) (Kavulich et al., 2013). Transient waves in the midlatitudes on Mars were found to behave in a similar way to those of the Earth. Baroclinic energy conversion was found in the low-land planitias of Mars, and barotropic energy conversion acted as a sink of EKE north of topographic features and a source in the planitias. Unfortunately, when compared to the Mars Analysis Correction Data Assimilation (MACDA), the GFDL simulation lacked sufficiently strong transient wave components with a wave number larger than 2.

Battalio et al. (2016) (hereafter B16) studied the energetics of transient waves in the northern hemisphere just before the winter solstice ($L_s = 200^\circ$ – 230°) during the MY 25 GDS and during two non-GDS years in MACDA. The transient wave energetics during the low opacity years of MY 24 and 26 was similar to those reported by Kavulich et al. (2013). However, during the MY 25 GDS, the number of wave packets during the $L_s = 200^\circ$ – 230° time was reduced to roughly half the number of those in MY 24 or 26. The reduction in the number of waves was caused by the altered mean state of the atmosphere due to the increased amount of atmospheric dust, which warmed the mid-atmosphere and cooled the surface, stabilizing the atmosphere to baroclinic instability. The stronger thermal forcing due to increased aerosol opacity also decreased the vertical wind shear in the lowest levels (between 500 and 800 Pa), further stabilizing the atmosphere against near-surface baroclinic instability. The amplitude of individual waves within wave packets during the dusty period did not decrease, as the loss of baroclinic energy conversion was offset by barotropic energy conversion from the time-mean flow to the waves. Barotropic energy conversion played a role in the dissipation of individual waves but was also a source of EKE in the time-mean,¹ which is somewhat different than the energetics paradigm of terrestrial waves, but it is consistent with previous work (Greybush et al., 2013).

2. Methods and data

2.1. MACDA

MACDA (v1.0) (Montabone et al., 2014) is a reanalysis of TES retrievals (Smith, 2004) from the Mars Global Surveyor mission during the period $L_s = 141^\circ$ MY 24 to $L_s = 86^\circ$ MY 27. The total dust opacities and thermal profiles are assimilated into the UK version of the LMD MGCM (Forget et al., 1999) using an analysis correction scheme (Lewis et al., 2007). The reanalysis is made available at 5° by 5° resolution at 25 sigma levels every two Mars hours.

The energetics described here covers four periods: pre-winter solstice ($L_s = 20^\circ$ – 50° and labeled “pre” in figures), winter ($L_s =$

¹ An error in Battalio et al. (2016) and in Kavulich et al. (2013) caused the BTEC to have the wrong sign (Battalio et al., 2018).

75°–105° and labeled “pause” in figures), post-winter solstice ($L_s = 150^\circ$ –180° and labeled “post” in figures), and summer ($L_s = 255^\circ$ –285°). We limit the calculation of energetics to periods of length 30° for two reasons: to avoid periods where TES retrievals were unavailable to be assimilated and to limit the analysis of energetics to short, representative seasons to ensure that the eddies are localized meridionally. Each of the four periods contains three individual years, except for the winter period that only covers MY 25 and 26. The post-winter solstice period in MY 25 is not shown, except in the vertical average, because it contains a long stretch when observations were unavailable, and it also covers the beginning of the MY 25 GDS that is partly initiated during a period not covered by observations. Additionally, the pre-winter solstice period of MY 24 begins at $L_s = 153.7^\circ$ instead of $L_s = 150^\circ$ due to the start time of the dataset. Finally, a radiometric error in TES spectra towards the end of the Mars Global Surveyor mission affects spectra from surfaces below about 210 K, which introduces an error in atmospheric temperatures of up to 3–5 K. This error occurs especially for temperature retrievals near the poles during and after MY 26 (Pankine, 2015, 2016).

We briefly discuss the average zonal properties of each of the seven periods listed above. For each of the three seasons, some inter-annual variability in the time-mean flow is found, with the most evident inter-annual variability due to the TES temperature retrieval errors after MY 26. Polar temperatures in MY 24 and 25 are colder than in the same season in either MY 26 or 27 (Fig. 1). This has an effect on the stability profiles and general circulation in MACDA, and where applicable, these biases in inter-annual differences between MY 24 and 25 to MY 26 and 27 will be noted. There are also key differences between the seasons. Focusing on the southern hemisphere, there is a strong westerly jet at all times of roughly the same magnitude (zonal wind contoured in Fig. 1), but the tilt of the jet is directed towards the pole with height during the pause seasons. The cross-section of zonal mean temperature shows a cold south polar region near the surface and warm equator and northern hemisphere. The meridional transition between the two areas is different between the seasons. During the pre- and post-pause seasons, the vertical temperature profile between 60° and 80°S and below 10 Pa is one favorable for baroclinic development (i.e., tilted away from the pole with height). However, during the pause period, the isotherms are tilted toward the poles. Such a signature was noted by Kuroda et al. (2007) as inhibiting baroclinic instability in the northern hemisphere at $L_s = 280^\circ$. The inhibition of baroclinic energy conversion by the vertical temperature profile was also established by B16 during the MY 25 GDS.

2.2. Eddy kinetic energy equation

The kinetic energy of atmospheric waves can be quantified in different ways. We use the form of the eddy kinetic energy equation derived by Orlandi and Katzfey (1991):

$$\frac{\partial}{\partial t} \langle K_e \rangle = \underbrace{-\langle \nabla \cdot \mathbf{v} K_e \rangle}_1 - \underbrace{\langle \nabla \cdot \mathbf{v}' \phi' \rangle}_2 - \underbrace{\langle \omega' \alpha' \rangle}_3 - \underbrace{\langle \mathbf{v}' \cdot (\mathbf{v}'_3 \cdot \nabla_3) \mathbf{v}_m - \mathbf{v}' \cdot (\mathbf{v}'_3 \cdot \nabla_3) \mathbf{v}' \rangle}_4 - \underbrace{[\omega' K_e]_s + [\omega' K_e]_t}_5 - \underbrace{[\omega' \phi']_s + [\omega' \phi']_t}_6 + \underbrace{\langle (Residue) \rangle}_7, \quad (1)$$

where the eddy kinetic energy per unit mass is defined as $K_e = \frac{1}{2}(u'^2 + v'^2)$. The geopotential is ϕ ; $\alpha = 1/\rho$ is the specific volume. The wave (eddy) components of the state variables are defined as deviations from the time-mean flow and are denoted with primes. The eddy components of the wind vector and the horizontal wind

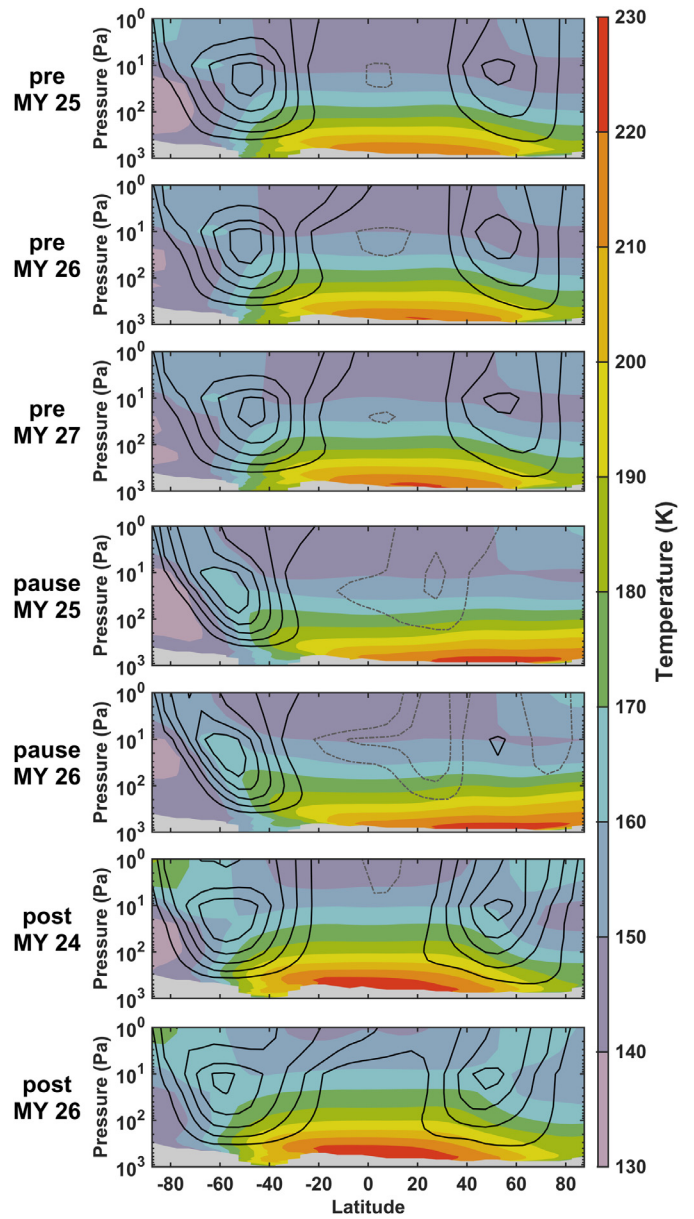


Fig. 1. Time-mean, zonal-mean temperature for three fall (pre: $L_s = 20^\circ$ –50°), two winter (pause: $L_s = 75^\circ$ –105°), and two spring (post: $L_s = 150^\circ$ –180°) periods. Contours are time- and zonal-means of the zonal wind every 15 m/s, with negative values dashed. Terrain is grayed.

vector are $\mathbf{v}'_3 = (u', v', \omega')$ and $\mathbf{v}' = (u', v')$, respectively. The time-mean flow is indicated with a subscripted m (e.g., \mathbf{v}_m). Terms with an overbar are time averaged. Each term in angle brackets is vertically averaged over the pressure coordinate. Terms 5 and 6 are integrated over the surface (s) or the top of the atmosphere (t), indicated by square brackets.

The seven terms on the right hand side of Eq. (1) represent processes that alter the rate of change of EKE. Terms one and two are transport terms and are EKE transport (ETRANS) and geopotential flux convergence (GFC), respectively. These two terms can be local sources or sinks of EKE, but their global integral at any time is zero. Terms three and four are energy conversion terms that can generate or remove EKE globally. In particular, term three is the baroclinic energy conversion term (BCEC), whereby available potential energy of the mean flow is converted to EKE, and term four is the barotropic energy conversion term (BTEC), whereby en-

ergy is converted from the mean flow to the waves. BTEC consists of two separate parts: the second term describes the interaction between eddies of differing frequencies and is sometimes called the cross-frequency eddy-eddy interaction term (e.g., Jiang et al., 2013). While small, this term is not negligible as it tends to be only roughly an order of magnitude smaller than the first term. The first term describes the interaction between the eddies and the mean flow, and it can be expanded as follows:

$$-\mathbf{v}' \cdot (\mathbf{v}'_3 \cdot \nabla_3) \mathbf{v}_m = \underbrace{-u'^2 \frac{\partial u_m}{\partial x}}_{4a} - \underbrace{u'v' \frac{\partial u_m}{\partial y}}_{4b} - \underbrace{u'v' \frac{\partial v_m}{\partial x}}_{4c} - \underbrace{v'^2 \frac{\partial v_m}{\partial y}}_{4d} - \underbrace{u'\omega' \frac{\partial u_m}{\partial p}}_{4e} - \underbrace{v'\omega' \frac{\partial v_m}{\partial p}}_{4f}. \quad (2)$$

The six terms are the zonal convergence of the zonal wind (4a), meridional shear of the zonal wind (4b), zonal shear of the meridional wind (4c), meridional convergence of the meridional wind (4d), vertical shear of the zonal wind (4e), and vertical shear of the meridional wind (4f). Generally, we have found that terms 4a, 4b, 4d, and 4e have the largest magnitude, with term 4c being somewhat smaller. Term 4f is roughly an order of magnitude smaller in absolute value than 4c.

Terms five and six are non-zero only because they are calculated at the lowest and highest pressure level where MACDA data are available rather than at the zero pressure level and the surface of Mars due to the conversion from sigma to pressure coordinates. The top of the atmosphere is considered to be at 1 Pa rather than 0 Pa, because the top three levels in the MGCM are sponge levels that do not provide realistic information about the state of the atmosphere. Term five is found to be two orders of magnitude smaller than the other terms and is neglected (B16). Term six is only one order of magnitude smaller than the other terms and is subsumed into term two. All references to the GFC term are defined as terms two plus six. Term seven is the residual and accounts for effects not described by the other terms, such as friction and dissipation, diabatic effects, or interpolation and numerical errors. The residual is found by directly calculating the left-hand side of Eq. (1), then subtracting the first six right-hand side terms.

The eddy components are filtered from the raw variables in two ways. Firstly, the time-mean state is defined as a 30-sol running mean for each variable – a choice that was also made by both Kavulich et al. (2013) and B16. Secondly, to ensure that the diurnal tide does not contribute to the transient eddy energetics, a Hamming-window filter is applied to remove temporal variability with frequency of 0.95–1.05 sol⁻¹ or frequency higher than 1.82 sol⁻¹ from the surface pressure, surface temperature, horizontal winds, and vertical temperatures. The removal of the 1.82 sol⁻¹ and higher frequency band prevents any semidiurnal tide signal, as MACDA has output of every two hours and 10/12 = 0.833.

MACDA does not contain vertical velocities, so vertical winds are derived using the quasi-geostrophic (QG) ω equation (B16). [For a more detailed description of the computation of QG- ω , see Battalio and Dyer, 2017.] In the midlatitudes, the QG approximation does hold on Mars, but B16 found that QG- ω occasionally had difficulty duplicating the vertical winds on a self-consistent model simulation. However, the QG part of the vertical motion was found to be the dominant contributor to the terms of the EKE equation. Topography is the strongest influence on QG- ω , particularly around Hellas Planitia, with strong descent on the western side of Hellas and on the leeward side of Tharsis (not shown).

The direct use of the divergence of the horizontal winds is avoided by rearranging the vector products of terms one and two of Eq. (1) so that, for example, the geopotential flux convergence term is found using a flux form as opposed to an advective form:

$$-\langle \nabla \cdot \mathbf{v}' \phi' \rangle = -\left\langle \frac{\partial (u' \phi')}{\partial x} + \frac{\partial (v' \phi')}{\partial y} \right\rangle. \quad (3)$$

Calculating terms one and two in this way is preferred as it eliminates an extra finite difference calculation (B16).

3. Time-averaged wave energetics

Each of the four periods investigated here cover four different regimes of transient eddy activity in the southern hemisphere. The wave amplitudes are the largest in the pre-winter and post-winter periods and are much smaller in the winter and summer periods.

3.1. Integrated EKE equation terms

3.1.1. Pre-winter solstice

The EKE equation terms for the pre-winter solstice season are shown in Fig. 2. Some inter-annual variability is present, but EKE is contained throughout the southern hemisphere highlands in the upper and midlatitudes and is present closer to the equator over Tharsis and particularly Solis Planum around the northern edge of Argyre. A noticeable amount of EKE exists from about 40°S, 120°E to the southeast to 70°S, 270°E. The poleward side of Hellas is also a preferred area of EKE. While Hellas and Argyre Planitia are generally lacking in EKE, EKE during MY 25 in Hellas Planitia is strong enough so that there is a near continuous band of EKE around the hemisphere, similar to the northern hemisphere pre-solstice period (B16). The activity in MY 25 in Hellas Planitia has been noted previously as a precursor to the MY 25 GDS (Strausberg, 2005). Slightly reduced EKE, particularly in MY 26, is partly due to changes in the polar temperature profile in the TES retrievals (Pankine, 2015, 2016).

BCEC (Fig. 2 second row) also shows inter-annual variability. The main area of BCEC is a crescent-shaped feature to the south of Tharsis and is strongest from 150° to 300°E, just upstream of Argyre. A second, smaller area of BCEC is between Argyre and Hellas Planitia. BCEC is negative inside or downstream of both basins. These regions are between 40° and 70°S, which is slightly more equatorward than the BCEC during the pre-solstice period of the northern hemisphere (B16). The difference in BCEC during the pre-pause MY 26 period and MY 25 and 27 periods is attributed to the degradation in quality of the TES retrievals (Pankine, 2015, 2016).

GFC (Fig. 2 third row) is strongest in MY 25 around the southern pole. In all years, there is GFC upstream of Tharsis and on the eastern flank of Hellas Planitia, with geopotential flux divergence on the western flank of the basin. The ageostrophic geopotential flux (AGF) convergence vectors are also shown:

$$(\mathbf{v}' \phi')_a = \mathbf{v}' \phi' - \mathbf{k} \times \nabla \frac{\phi'^2}{2f(y)}, \quad (4)$$

where $f(y)$ is a latitudinal varying Coriolis parameter (Orlanski and Sheldon, 1993). The strong GFC near the south pole in MY 25 is connected to anomalous AGF vectors compared to MY 26 and 27. Between 120° and 180°E, AGF vectors are away from the pole and converge south of 70°S, but in MY 26 and 27, vectors are more zonal near the pole, with some circulation around the southern side of Tharsis and into Argyre. In all three years, there is convergence of fluxes from the south to north, west of Argyre. Convergence over Tharsis itself is associated with northwesterly vectors, which direct some energy towards the upwind side of the pre-pause storm track. The dipole in Hellas Planitia is due to strong divergence directed toward the convergence on the eastern side.

ETRANS (Fig. 2 fourth row) is of similar magnitude to the GFC term. The strongest areas of ETRANS are in Hellas Planitia, with a

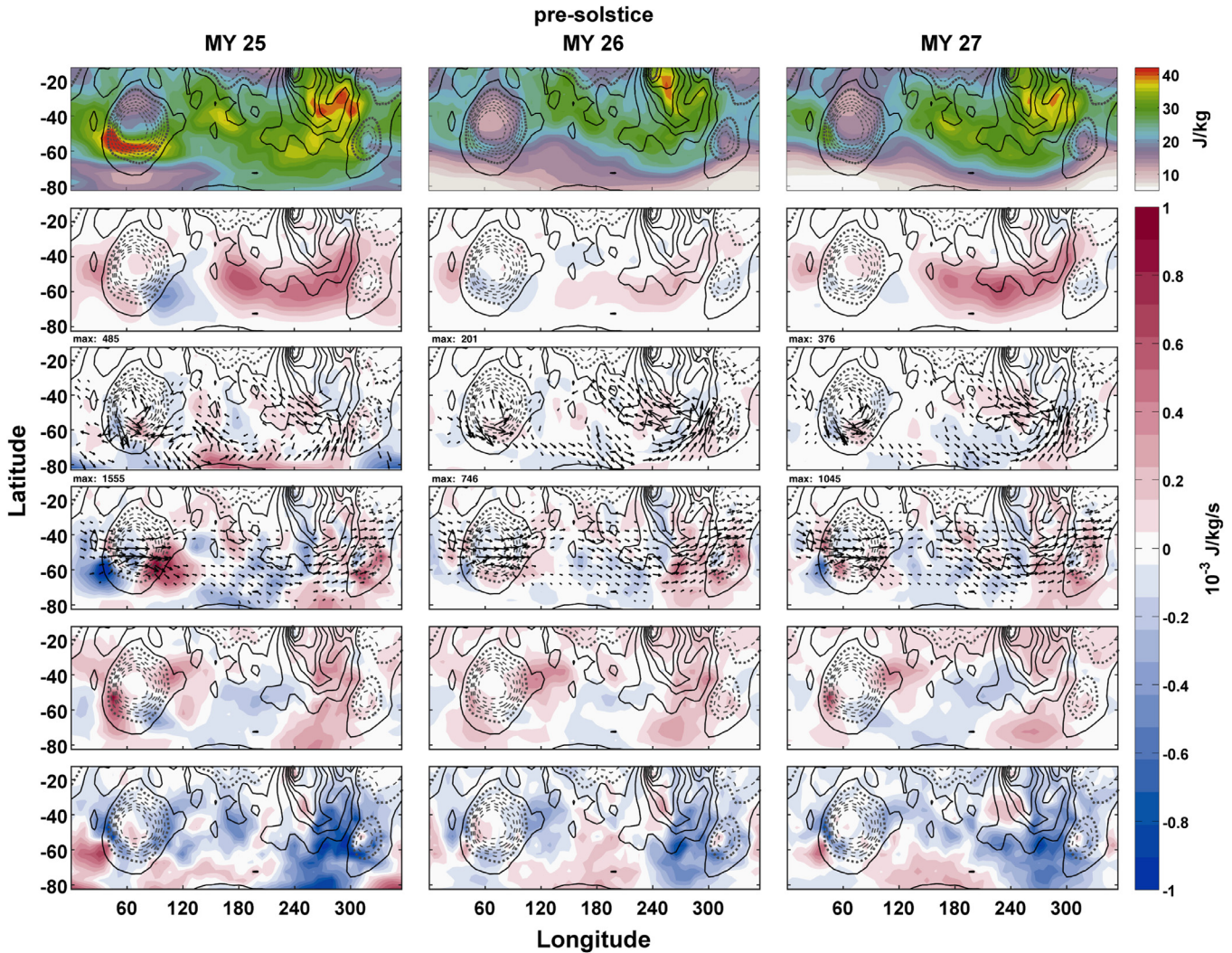


Fig. 2. Time-mean, pressure-weighted vertical averages of the terms in the eddy kinetic energy equation for $L_s = 20^\circ\text{--}50^\circ$ for MY 25 (left column), MY 26 (center column), and MY 27 (right column). Shown is the eddy kinetic energy (top), baroclinic energy conversion (second row), geopotential flux convergence (third row), eddy kinetic energy transport (fourth row), barotropic energy conversion (fifth row), and the residue (bottom). Vectors are ageostrophic geopotential flux (m^3/s^3 , third row) and eddy kinetic energy transport flux (m^3/s^3 , fourth row). The maximum magnitudes for AGF and ETRANS vectors are listed at the top left of the respective panels. Contours are surface elevation in 1000 m increments, with dashed values below the mean geoid and the mean geoid in bold.

positive area on the eastern side and a negative area on the western side. The ETRANS flux, $\mathbf{v}K_e$, is mostly zonal and strongest between 40° and 70°S . The ETRANS flux dips southward and accelerates around Tharsis, and more importantly, EKE is transported from the southwestern side of Hellas, accelerated through the basin, then deposited on the southeastern side.

BTEC shows less inter-annual variability, but unlike GFC and ETRANS, BTEC (Fig. 2 fifth row) has a positive region on the western side and a negative region on the southeastern side of Hellas Planitia. There is also a positive region on the northeast side of Hellas and another along and poleward of Tharsis itself. The areas of positive BTEC associated with topography indicate a result similar to the pattern found in the northern hemisphere – that eddies traveling around topography gain energy from the mean flow (B16 and Footnote¹).

The residue term (Fig. 2 bottom row) shows some variability in the midlatitudes but less variability near the pole. There are positive regions of the residue on the southwestern flank of Hellas and near the pole between 100° and 200°E and negative regions on the eastern side of Hellas and throughout flat highlands of Terra Cimmeria and Terra Sirenum ($150^\circ\text{--}300^\circ\text{E}$). The broad swaths of negative residue between 220° and 300°E indicate that the processes

amalgamated into this term, especially friction, are important local sinks of EKE at the end of the baroclinic storm track.

3.1.2. Solstices

The EKE equation terms are the weakest during the solstice periods. The EKE during the winter solstice (Fig. 3 left and middle columns, top row) is confined to Tharsis. The shape of the EKE field (Fig. 3 right column, top row) in the summer average is more like in the fall and spring than winter; however, the magnitude is much smaller.

BCEC (Fig. 3 second row) has a weak positive area along the southern edge of Tharsis in winter and a positive area over Tharsis in summer. In winter, Hellas Planitia has prevalent negative BCEC. BTEC (Fig. 3 fifth row) is positive throughout the southern hemisphere in winter and is negligible in summer, suggesting that any transient waves around winter solstice are barotropic in nature.

Inter-annual variability dominates GFC and ETRANS. There are no specific areas of GFC or ETRANS common to all three years, as would be expected for periods when the energetics is weak (Chang, 2001). GFC is smaller in magnitude than ETRANS for all three periods. The patterns of AGF and ETRANS fluxes in the winter solstice period are similar to those in the pre-pause period

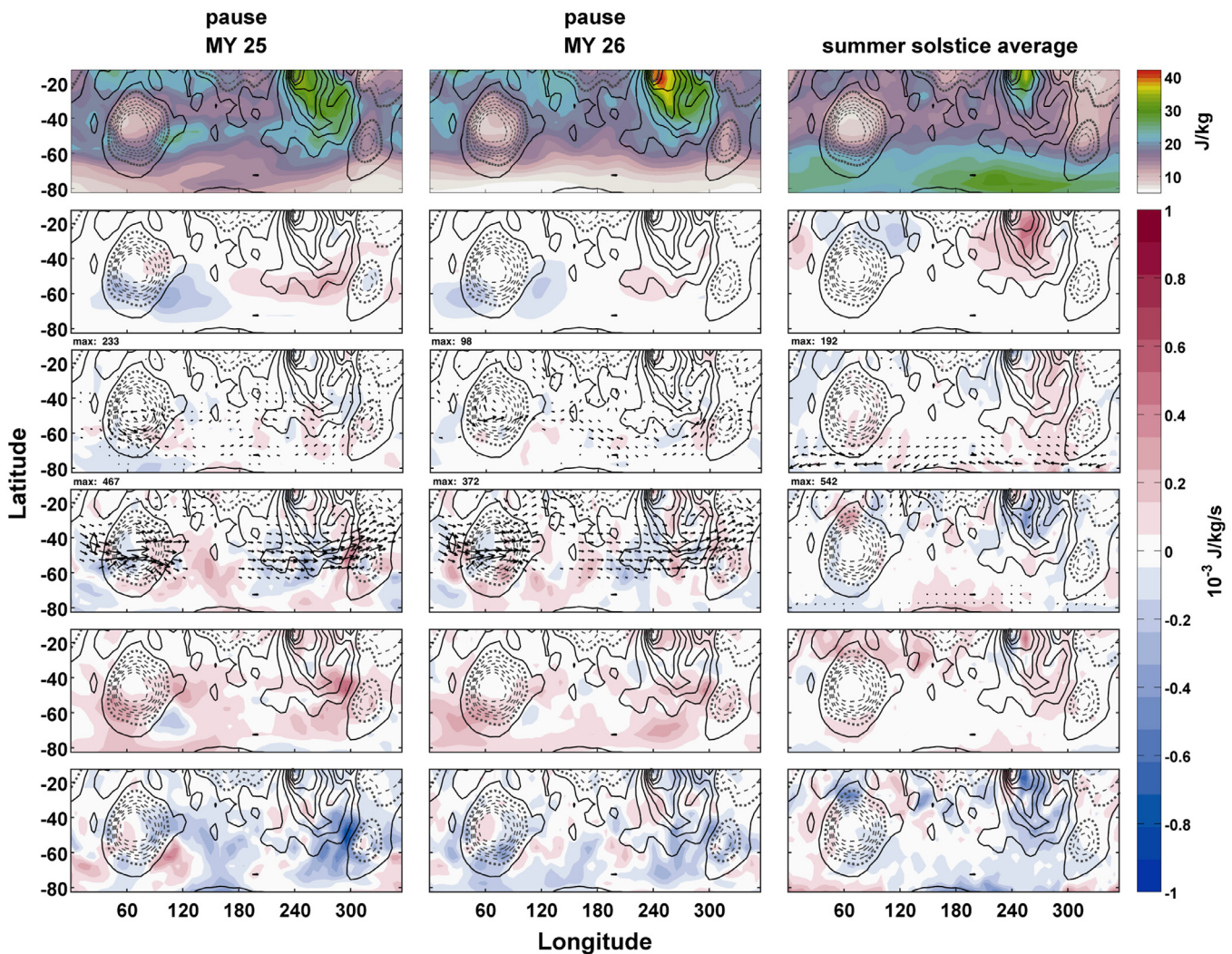


Fig. 3. As in Fig. 2 but for the winter pause period for MY 25 and 26 and the average summer period.

but are weaker in amplitude. The residue term is mostly negative in winter and summer midlatitudes. The magnitude of the residue is largest along the southeastern tip of Tharsis.

3.1.3. Post-winter solstice

The terms of the EKE equation during the post-winter solstice period are shown in Fig. 4. There is great variability between the three years, noting that we mostly discount the post-pause period in MY 25, as it contains roughly 10 degrees of areocentric longitude where the model ran freely, as well as the 2001 GDS. The intense lifting during the GDS dramatically increased the EKE compared to that in MY 24 or 26. Furthermore, the EKE during MY 26 is reduced due to the TES south pole temperature degradation. EKE in the post-solstice period is higher closer to the southern pole than in the pre-pause period, with the highest values located in the 50°–70°S latitude band. The longitudinal distribution also differs from the pre-pause period. There is little to no EKE downstream of Hellas as there is in the pre-pause period, and there is no local maximum of EKE over Tharsis in MY 24 or 25 in the post-pause period. In MY 24 and 26, the highest EKE is shifted away from Solis Planum in the pre-pause period to the south, just upstream of Argyre. There is also EKE directly upstream of Hellas in both years. For none of the three periods shown is there a noticeable amount of EKE from north of Hellas and near the equator to the southeast towards the southern tip of Tharsis as in the pre-

solstice period. This northwest to southeast storm zone in the pre-pause period, with a local maximum around 150°E, does not occur in the post-pause period.

BCEC during the post-solstice period (Fig. 4 second row) is similar to that during the pre-solstice period, with a maximum south of Tharsis and a secondary maximum upstream of Hellas. BCEC is more concentrated near Argyre in the post-pause period rather than wrapping around the southwestern edge of Tharsis as during the pre-pause period. BTEC (Fig. 4 fifth row) is much weaker than BCEC and is the weakest of all the terms, with its most positive values south of Tharsis and negative values in Terra Cimmeria and Terra Sirenum, similar to the situation in the pre-solstice period.

GFC (Fig. 4 third row) is the strongest in Hellas Planitia, with divergence on the western side and convergence on the eastern side. A weak area of geopotential flux divergence resides at the southern tip of Tharsis, with GFC on the eastern side of Argyre in MY 24. ETRANS (Fig. 4 second row) is spatially similar to, but stronger than, the GFC term. AGF vectors consist of a broad area of counterclockwise circulation trapped between Hellas to the west and Tharsis and Argyre to the east. The strongest area of circulation is on the eastern side. AGF fluxes serve to recirculate EKE around to the beginning of the storm track, which does not occur in the pre-pause period, providing a partial explanation for the increased intensity of post-pause eddies. The maximum magnitude of the AGF fluxes (labeled above each panel in Figs. 2–4) is largest

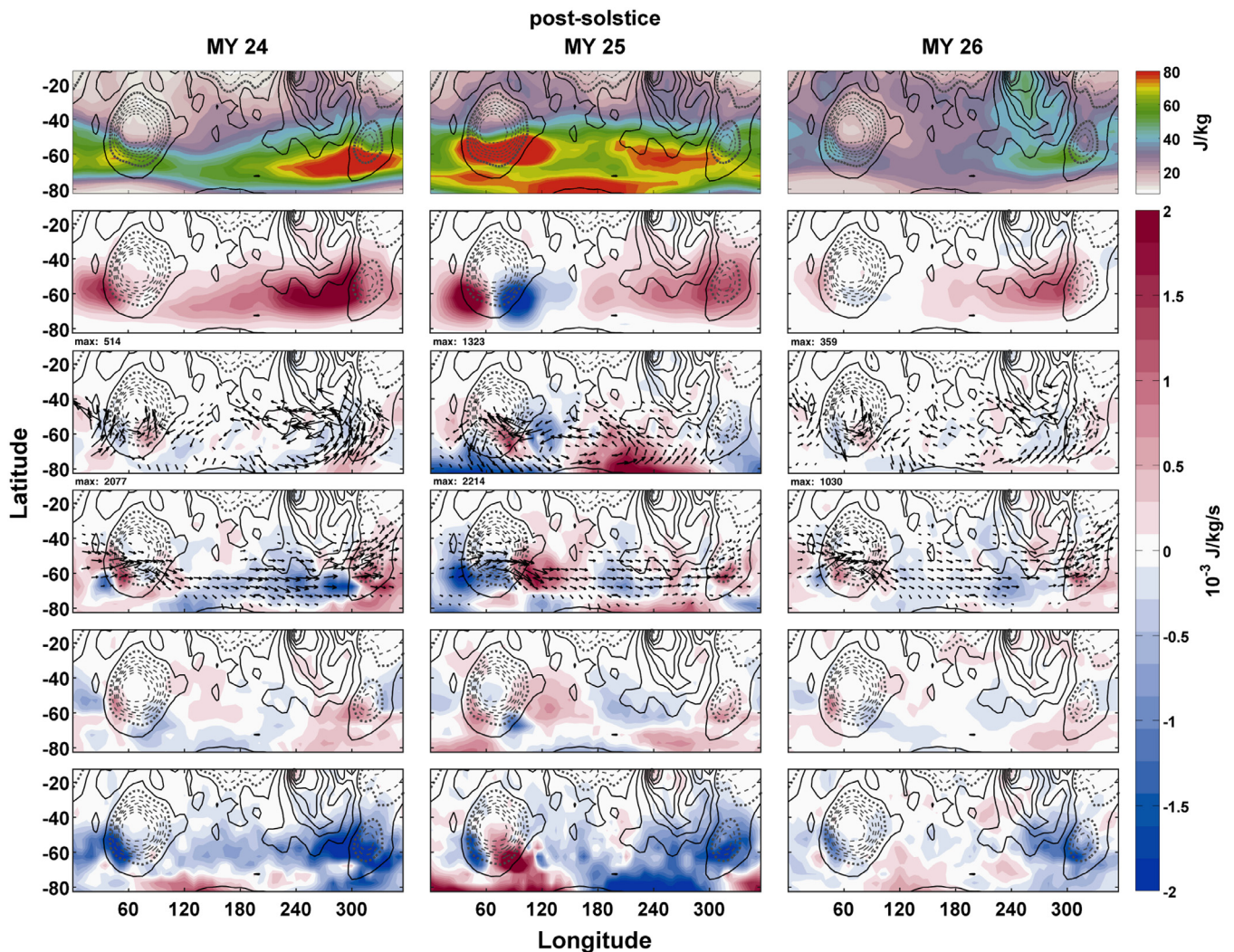


Fig. 4. As in Fig. 2 but for the post-pause period ($L_s = 150^\circ\text{--}180^\circ$) for MY 24 (left column), MY 25 (center column), and MY 26 (right column).

in the post-pause period. ETRANS flux vectors are zonal as in the other two periods but are stronger and are closer to the pole due to the jet stream migration toward the pole and a tightened polar vortex (Waugh et al., 2016).

The residue term is the strongest sink of EKE on average, with broadly negative areas in both MY 24 and 26 south and east of Tharsis and in Argyre and Hellas Planitia. This indicates that friction and dissipation are the largest local sinks of EKE in the southern hemisphere post-solstice period.

3.2. EKE

EKE is shown for each of the seven investigated periods in Fig. 5, with the zonal average at left and the meridional average at right. EKE during the pre-pause period (top three rows) is of intermediate intensity. There is uniform EKE at the upper-levels throughout the midlatitudes, with values up to 100 J/kg at 10 Pa . Only weak EKE is found below 200 Pa , with a magnitude of no more than 25 J/kg . EKE during the pause periods (rows four and five, respectively) is the weakest. EKE increases monotonically with height at all longitudes and latitudes. The post-pause period (bottom two rows) has the strongest average EKE. The zonal maximum of EKE poleward of 60°S lines up with the area of the westerly jet maximum.

3.3. BCEC

BCEC is shown with color shades in Fig. 5. BCEC is a source of EKE in the pre- and post-pause periods and is strongest in the post-pause period, with the weakest BCEC occurring in the pause period. Positive BCEC is found in the pre- and post-pause periods between 30° and 75°S . BCEC during the post-pause period is positive between 400 and 50 Pa but is shallower and weaker in the pre-pause period. This leads to BCEC maxima being roughly the same height above the ground, as the surface pressure is lower during the post-pause period. Meridionally, there are two preferred regions of positive BCEC. The stronger area lies between 120° and 300°E , while the weaker area is just east of Hellas Planitia. During the pause period, there is an area of negative BCEC near 100 Pa above Hellas, and in non-pause times, this area of negative BCEC is smaller and weaker. There is great inter-annual variability in the three seasons. During the pre-pause period, the strongest BCEC is found in MY 27, and the strongest BCEC during the post-pause period occurs in MY 24. BCEC in the pre- and post-pause periods in MY 26 is reduced due to the anomalously warmed polar temperatures in TES.

As the manifestations of energy conversion in baroclinic instability, the zonal and meridional heat fluxes are considered, first in the zonal average (Fig. 6 left column). The strongest heat fluxes are found during the post-pause period, with the weakest during the

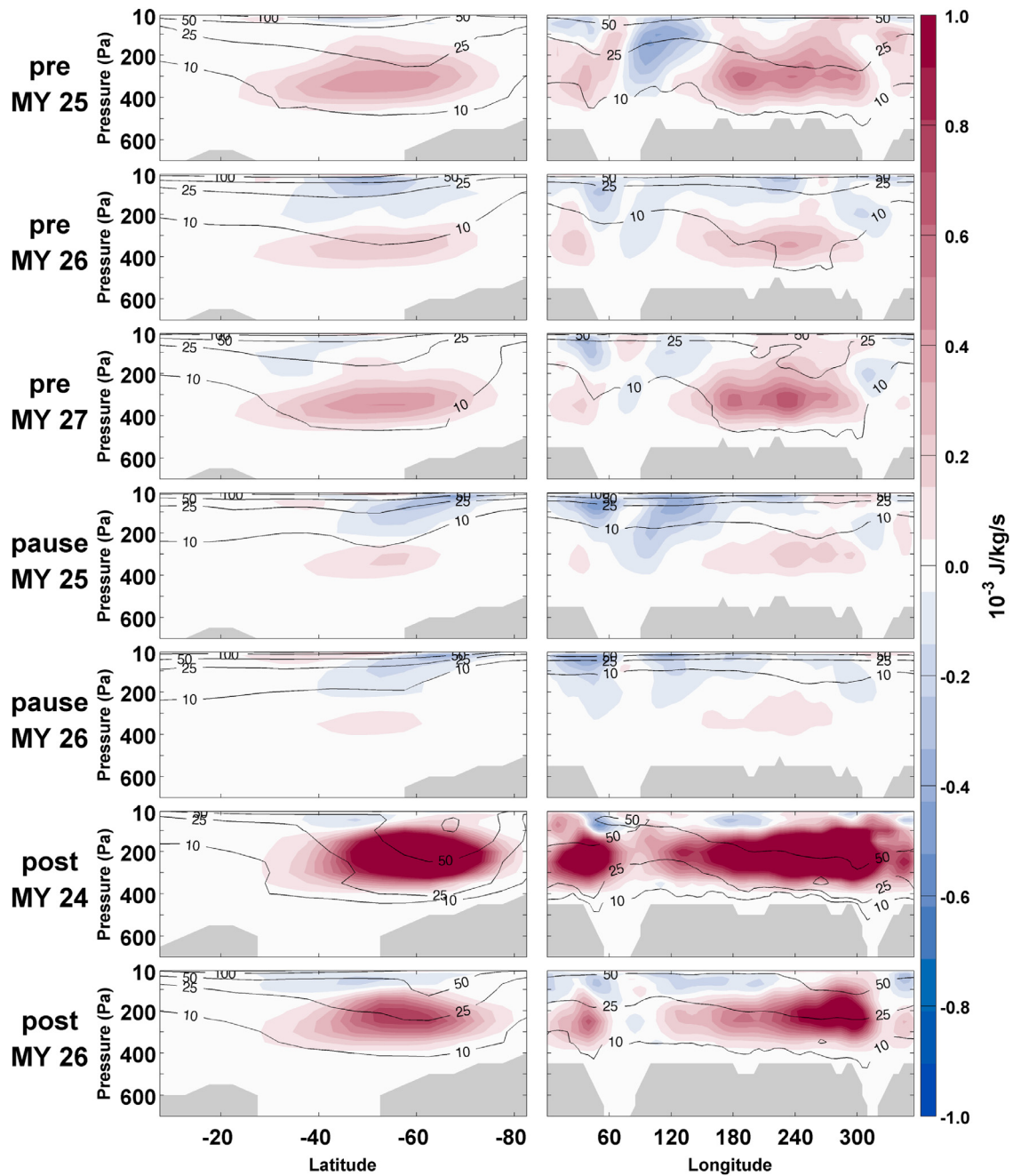


Fig. 5. Time-averaged baroclinic energy conversion during three fall (pre: $L_s = 20^\circ\text{--}50^\circ$), two winter (pause: $L_s = 75^\circ\text{--}105^\circ$), and two spring (post: $L_s = 150^\circ\text{--}180^\circ$) periods in the zonal (left column) and $52.5^\circ\text{--}82.5^\circ\text{S}$ meridional (right column) average. Contours are average zonal EKE (J/kg). Terrain is grayed.

pause period. The strongest vertical heat flux ($-\omega'T'$) (contours) is slightly above the strongest meridional heat flux ($-v'T'$) (shading). The zonally averaged meridional heat flux is negative above 100 Pa in each of the pre-pause, pause, and the MY 26 post-pause period. This suggests that the negative BCEC at those levels is caused by the transport of heat away from the pole. All meridionally averaged heat fluxes are positive in all periods between Hellas and Argyre. In agreement with the results of Mooring and Wilson (2015), the meridional heat fluxes are the strongest in the post-pause period. The area of negative vertical heat flux on the eastern side of Hellas is the main contributor to the negative BCEC in that area, as the same pattern is not present in the meridional heat fluxes. The negative meridional heat flux, however, contributes to the negative BCEC above 100 Pa in all periods except for the post-pause in MY 24. Weaker heat fluxes in MY 26 are due to the warmed polar

regions in TES retrievals that reduce the vertical and meridional temperature gradients (Fig. 1). While there are strong meridional heat fluxes in Hellas and Argyre Planitia, there are no vertical heat fluxes in either basin, suggesting that the heat transport is due to barotropic waves.

3.4. BTEC

BTEC is usually found to be a global sink of EKE in the time-average terrestrially (e.g., Chang and Orlandi, 1993; Orlandi and Sheldon, 1995) and in the lower levels in some studies of Martian energetics (Wang et al., 2013; Wang and Toigo, 2016); however, recent work has indicated that the paradigm of barotropic stabilization is a bit of a simplification, with BTEC at times contributing positively to EKE in the terrestrial midlatitudes (e.g.,

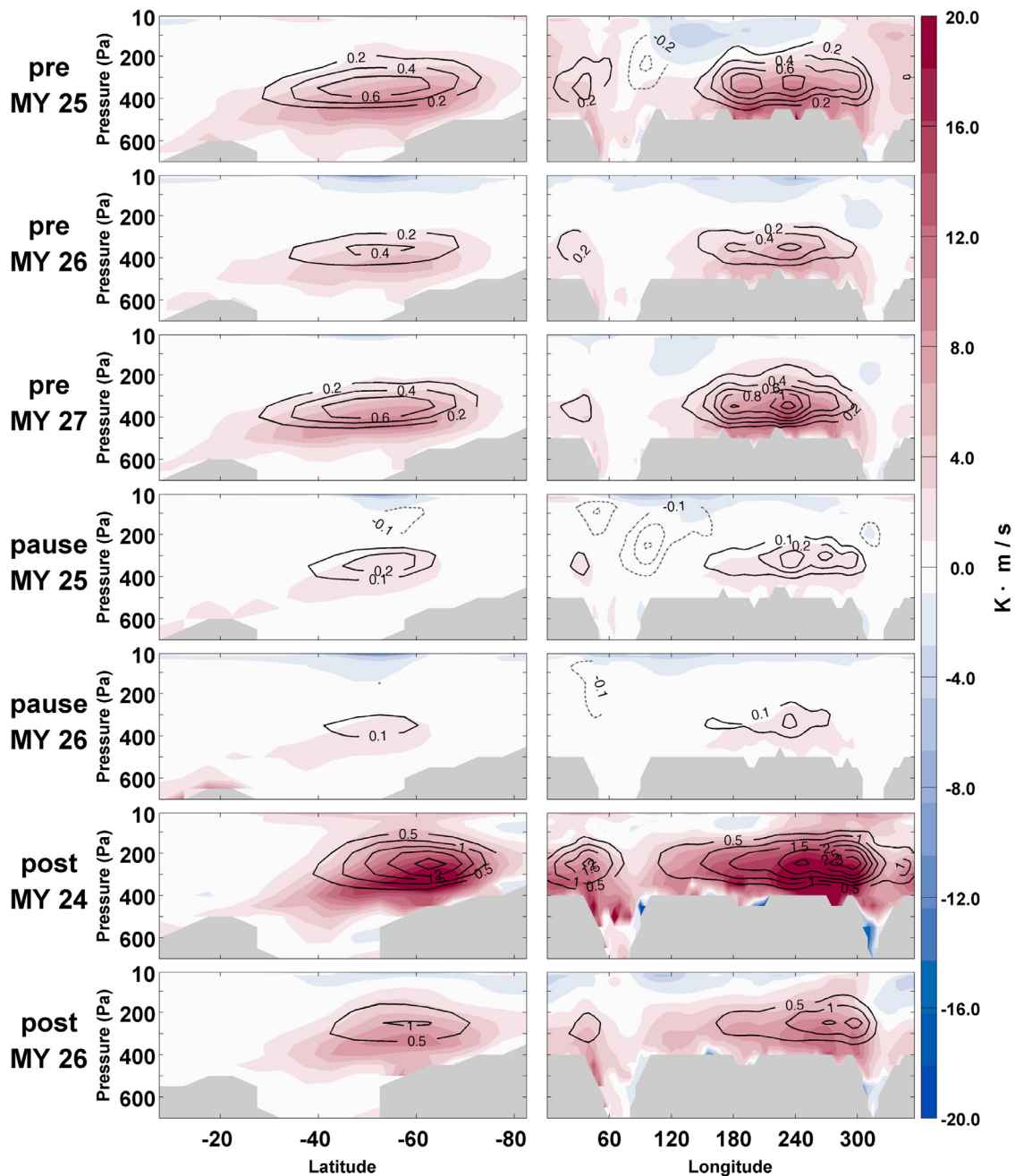


Fig. 6. For the same time periods as in Fig. 5 but for the zonal (left) and meridional (right) average of the meridional heat fluxes. Contours are averaged vertical heat flux (10^{-4} K · Pa/s). Terrain is grayed.

Chang, 2001; Chang et al., 2002; Ahmadi-Givi et al., 2014). Positive BTEC is also found in the northern hemisphere of Mars in the upper levels (Barnes et al., 1993; Greybush et al., 2013; Kavulich et al., 2013; Wang et al., 2013; Wang and Toigo, 2016; Battalio et al., 2016). The same is found during most periods in the southern hemisphere (Fig. 7). During the pre-pause period, there is a positive area of BTEC near 10 Pa between 20° and 50° S. This corresponds to the time when the position of the jet is nearest to the equator (Fig. 7 contours), which indicates a transfer of kinetic energy from the mean flow to the transients. Negative BTEC is found closer to the surface at 200 Pa, as in Wang and Toigo (2016). During the pause, the positive region of BTEC is further south, between 40° and 60° S. The area of positive BTEC in the post-pause period is much weaker and smaller, and the region of negative

BTEC is stronger compared to the pre-pause period. This is contrary to the idea of a strictly angular momentum conserving or a strictly eddy-driven jet, as BTEC switches sign from the pause period to the post-pause period. Instead, although it is accepted that the jet is primarily subtropical by nature and caused by the conservation of angular momentum from the Hadley circulation (Read et al., 2015), the jet occasionally takes characteristics of an eddy-driven jet like that in the high latitudes of Earth. This situation is equivalent to the northern hemisphere on Earth during mid-winter when the subtropical (angular momentum conserving) jet caused by the Hadley circulation merges with the northern eddy-driven jet (Lee and Kim, 2003). Waves on Mars can extract energy from the zonal-mean circulation without the jet losing momentum because it is driven by the Hadley circulation. This result fits

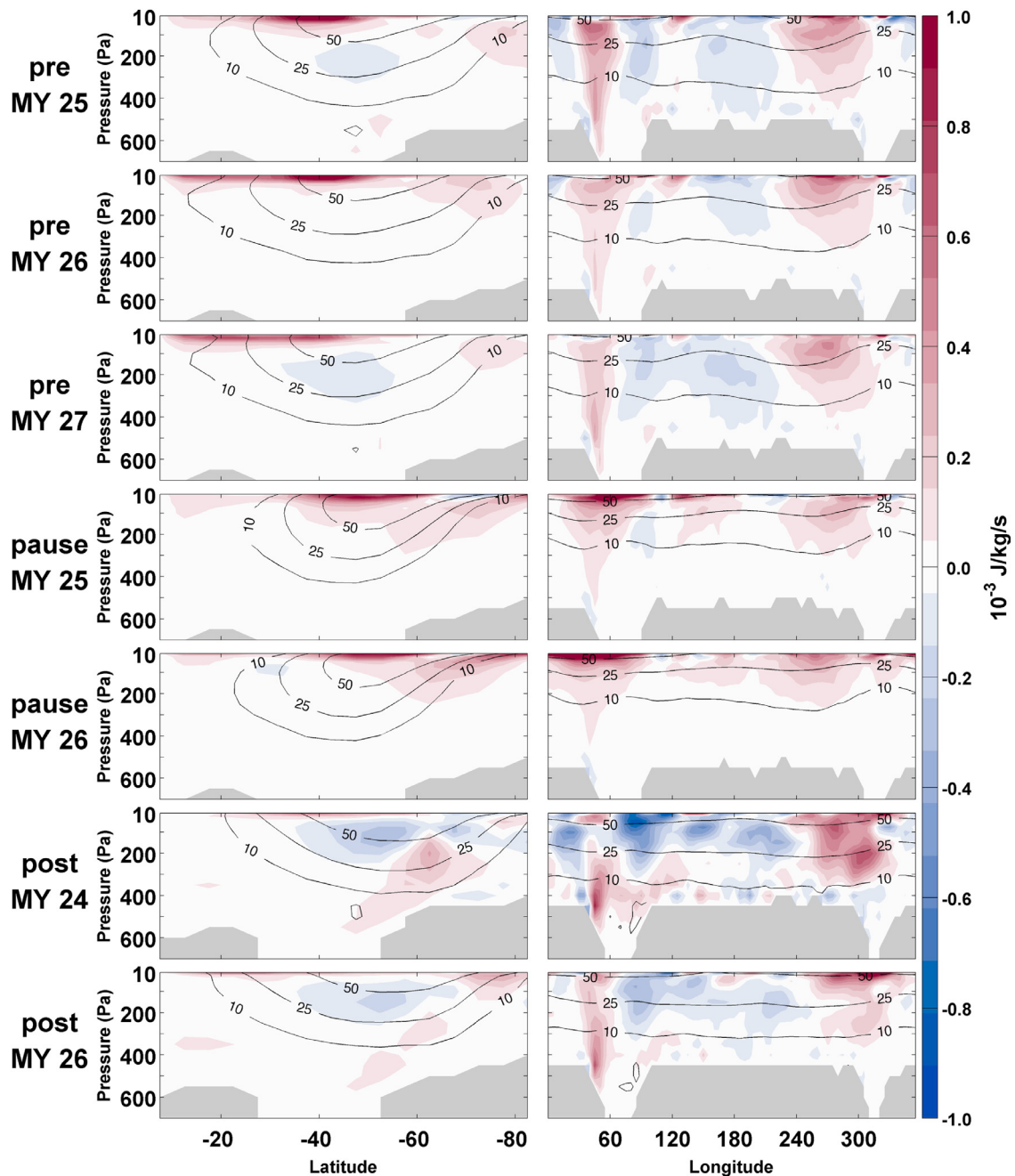


Fig. 7. For the same time periods as in Fig. 5 but for barotropic energy conversion. Contours are average zonal wind (m/s). Terrain is grayed.

within the context of the polar annulus of potential vorticity being barotropically unstable and driven by diabatic heating (Vaughan et al., 2016; Toigo et al., 2017). This also explains why there remains some limited wave activity during the pause period despite the lack of BCEC; the atmosphere is barotropically unstable.

In all seasons, the meridional shear of the zonal wind [Eq. (2) term 4b] and meridional convergence of the meridional wind [Eq. (2) term 4d] are the largest positive terms (not shown). Eddies are strengthened due to the conversion from the meridional shear of the time-mean zonal winds and due to wave accumulation in the meridional direction. In the pre-pause and post-pause seasons, the vertical shear of the zonal wind [Eq. (2) term 4e] and to a lesser extent the zonal convergence of the zonal wind [Eq. (2) term 4a] causes the negative BTEC region in the zonal average

(not shown). Qualitatively, the wave accumulation terms [Eq. (2) terms 4a and 4d] cancel, and the shear terms dominate. These results generally agree with energetics work in the subtropical terrestrial atmosphere (Seiki and Takayabu, 2007; Zhan et al., 2011; Tsou et al., 2014). Additional analysis of the BTEC term is left for future work.

The meridional distribution of BTEC is fairly uniform across all seven investigated periods. A barotropic source of EKE is located upstream of both Argyre and Hellas Planitia, but BTEC is strongest at the surface in the post-pause period and strongest aloft in the pause period. BTEC is a sink of EKE in the region of highest EKE and BCEC, between the two deep basins and above 300 Pa in the pre- and post-pause periods. BTEC is a source of EKE throughout that area in the pause period, with few barotropic sinks.

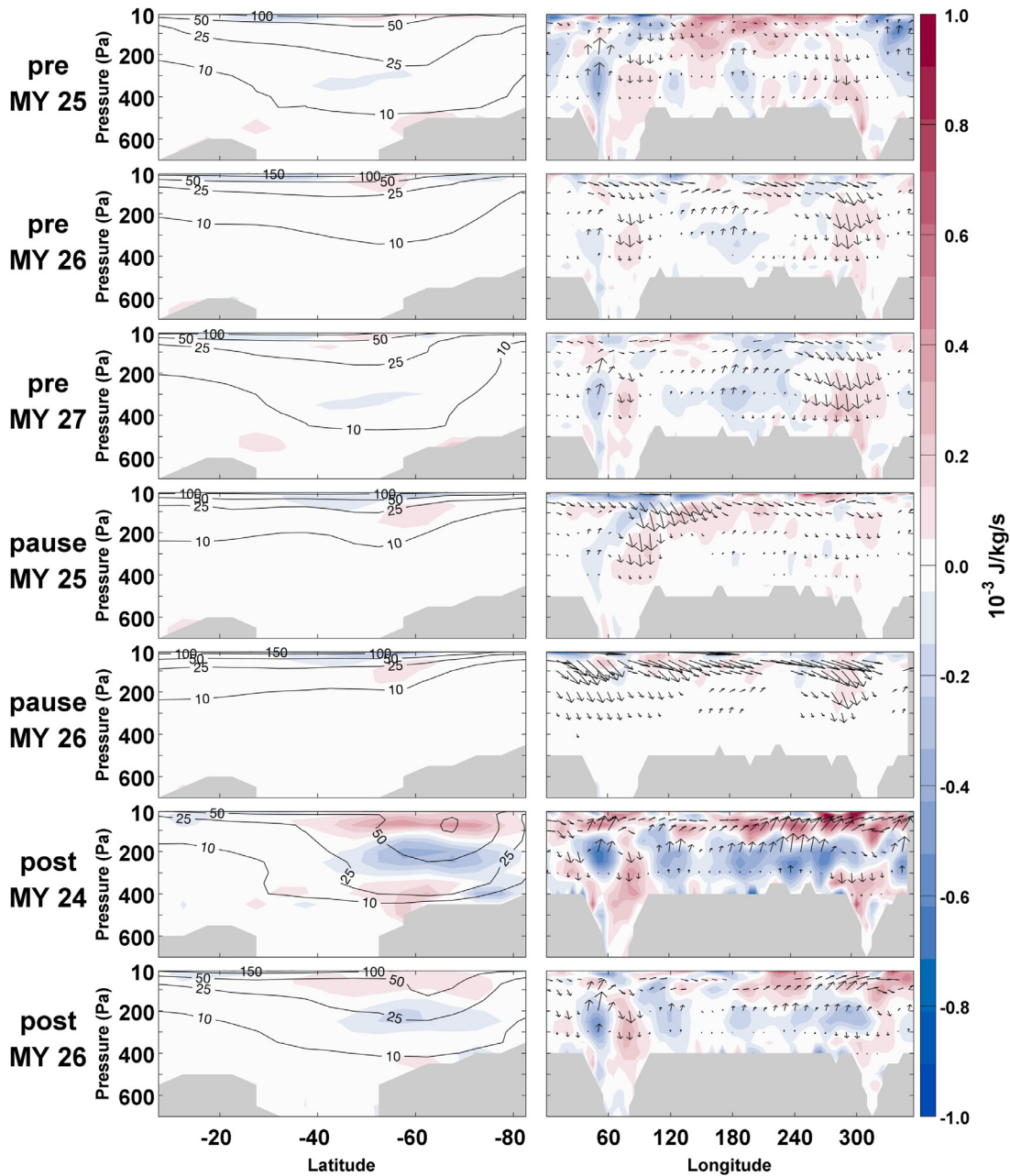


Fig. 8. For the same time periods as in Fig. 5 but for geopotential flux convergence. Vectors are ageostrophic geopotential flux, with motions in the vertical direction multiplied by 10^4 . Contours are average zonal EKE (J/kg). Terrain is grayed.

3.5. GFC

GFC has the largest magnitude in the two post-pause periods but is somewhat weaker than the two energy conversion terms (Fig. 8). Near the surface and south of 60°S , there is a shallow layer of positive GFC. Above that and between 300 and 150 Pa, there is a layer of geopotential flux divergence, with another layer of positive GFC extending up to 10 Pa. The strongest BCEC (Fig. 5) is collocated with the areas of geopotential flux divergence, and the areas of negative BCEC correspond to GFC.

In the meridional average, there is positive GFC near the surface on the eastern side of Hellas Planitia and just upstream of Argyre Planitia. Both of these regions have AGF flux vectors that are directed towards the surface, with the strongest fluxes in the pause periods. [Note: to indicate vertical direction of the fluxes, the vertical component of the vectors has been multiplied by 10^4 .] There

is geopotential flux divergence along the surface in the highlands between the two large impact basins, and in these areas, the AGF vectors are directed upwards into the top layer of positive GFC.

3.6. EKE transport

ETRANS is generally the stronger of the two transport terms. For the pre-pause and pause periods, the zonal mean of the ETRANS term is small except for above 100 Pa (Fig. 9 left column). Positive transport is indicated north of 40°S in the pre-pause periods and further north during the pause. During the post-pause periods, ETRANS has a couplet between 10 and 400 Pa, with negative advection at 70°S and positive advection at 55°S , indicating that in the meridional direction, this term serves to transport EKE equatorward and out of the main westerly jet, similar to the situation in the northern hemisphere (B16). The small magnitude of the zonal

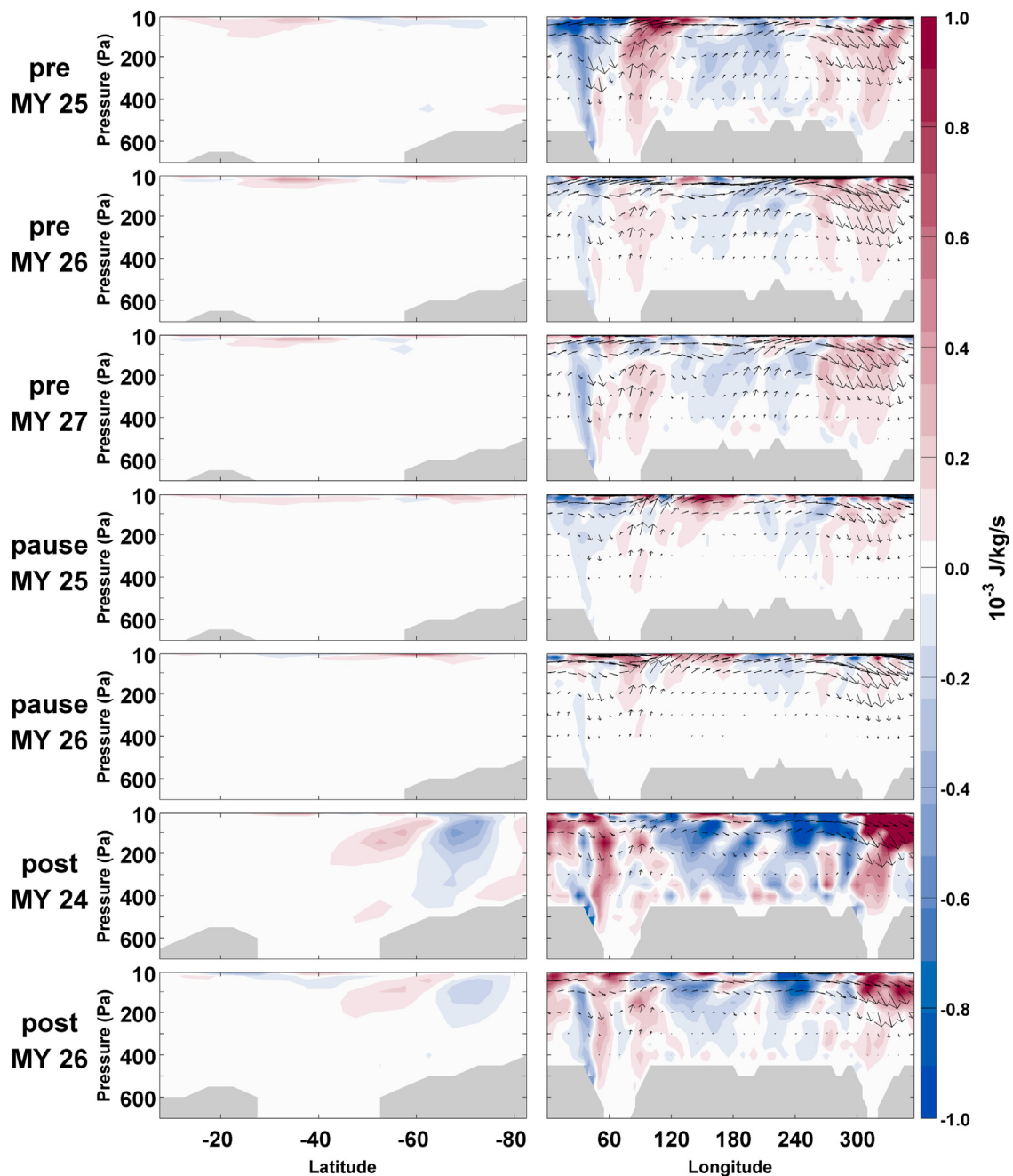


Fig. 9. For the same time periods as in Fig. 5 but for ETRANS. Vectors are EKE flux, with motions in the vertical direction multiplied by 10^4 . Contours are average zonal wind (m/s). Terrain is grayed.

mean is due to the near cancelation of terms in each zonal band, as the meridional mean shows vertical alignment of positive and negative areas, unlike the GFC term, which has vertical layering. In all periods, there is a visible wave number 2 pattern in both ETRANS and the ETRANS fluxes. [Again, the vertical component of the vectors has been multiplied by 10^4 .]

4. Case studies

Typical transient waves from the pre-pause, pause, and post-pause periods are compared to contrast their intensity and development.

4.1. Pre-pause example wave

A pre-pause wave is considered from MY 27 during $L_S = 47.90^\circ\text{--}49.94^\circ$, for which the EKE equation terms are shown in Fig. 10. The evolution of this wave is similar to several others in the pre-pause period in MY 27 as shown in a Hovmöller diagram for v' (Fig. 11) [The selected wave is labeled A in the diagram]. The wave has a period of 10 sols, with a distinct wave number 4 pattern. The wave is similar to other waves at this time and year, which is in a long-period, high-wave number regime that is not observed in the northern hemisphere, as waves above wave number 3 have little amplitude in the northern hemisphere (Wang and Toigo, 2016). The wave starts to develop around 160°E by GFC (Fig. 10 middle

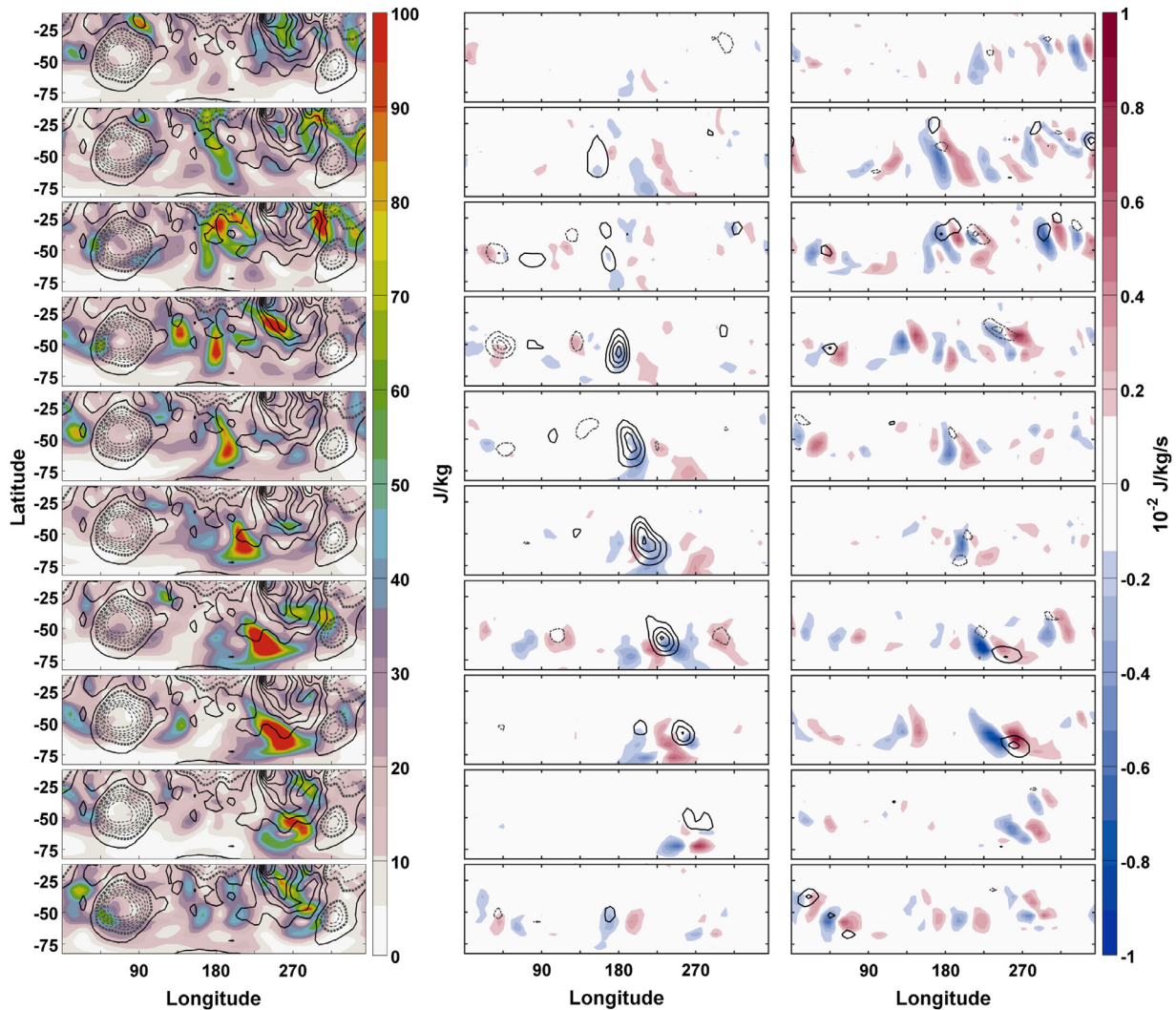


Fig. 10. Progression of a wave development during the time period MY 27 $L_s = 47.90^\circ$ – 49.94° . Time increases from top to bottom by 0.5 sol from one row to the next. Shown are (left) EKE (color shades) and topography (contours with 1000 m intervals) with negative values dashed, (middle) GFC (color shades) and BCEC (contours with 0.01 J/kg/s intervals) with negative values dashed, and (right) EKE advection (color shades) and BTEC (contours with 0.01 J/kg/s intervals) with negative values dashed.

column). Concurrently, an area of weak BCEC develops (middle column, contours) along a wave packet marked by a pattern of alternating positive and negative values of ETRANS (right column). In the third time-step, geopotential flux divergence further intensifies in the eastern region of positive BCEC and turns negative in the western region of BCEC on the western flank of Hellas. Baroclinic growth and the eastward transport of EKE by ETRANS and GFC lead to an amplification and the eastward extension of the wave packet. Finally, the kinetic energy of the wave packet dissipates, though is maintained in time-steps seven and eight by BTEC. The beginnings of the next wave development are evident at 180°E . The wave shares some similarities to that of northern hemisphere waves in that the EKE maximum is collocated with the BCEC maximum and the wave is transported by GFC and ETRANS (B16). However, there are several key differences. GFC has two dipoles surrounding the BCEC during the peak EKE, BTEC is never a strong sink of EKE, and the wave track is localized in the zonal direction. Waves achieve a heightened amplitude between 140 and 270°E but decrease in amplitude elsewhere only to re-amplify again when crossing the southern highlands between Hellas and Argyre (Fig. 11).

4.2. Post-pause

The selected post-pause wave evolves during $L_s = 166.31^\circ$ – 168.82° in MY 24 (Fig. 12) [labeled B in Fig. 11]. This wave is an example of baroclinic downstream development and is one of the stronger MY 24 waves. It is a 4-sol, wave number 3 development and so is similar to many northern hemisphere waves, especially the example of downstream baroclinic development highlighted in the northern hemisphere in Fig. 14 of B16, only with weaker energetics [a 300–400 J/kg EKE max versus a typical 700–800 J/kg EKE max with northern hemisphere waves (B16)]. At the initial time, there is a wave train that extends around the entire latitude circle, but the wave that later leads to the development of a more energetic wave packet (Fig. 12 left column) is located to the east of Argyre. A combination of GFC (Fig. 12 middle column) and ETRANS (Fig. 12 right column) transports EKE eastward from this region. The most energetic section of the wave packet reaches the eastern side of Hellas in 1.5 sols. The eastward expanding wave packet triggers EKE. GFC (fifth row from the top, middle column, contours) further energizes the eastward expanding wave packet, triggering intense BCEC downstream (from sixth to eighth row from

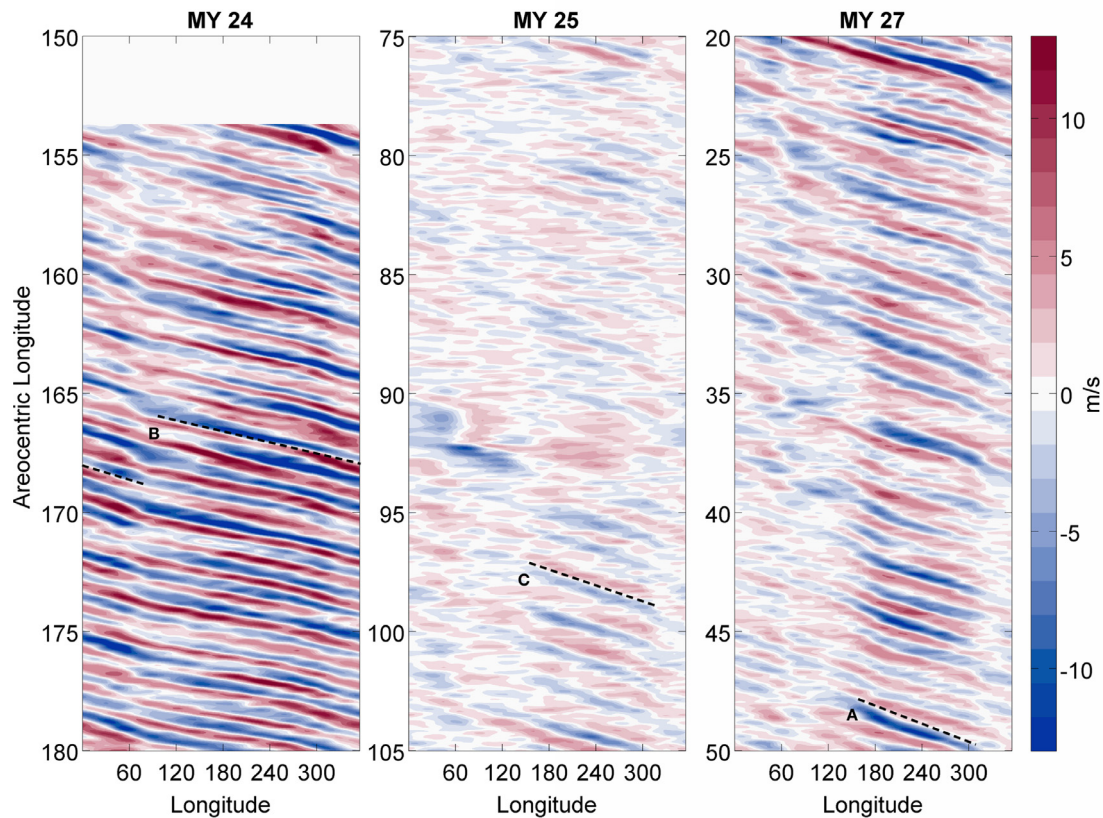


Fig. 11. Hovmöller diagram of the eddy meridional wind at 300Pa for three periods in the MACDA dataset averaged between 57.5° and 82.5°S. See text for explanation of letters A, B, and C.

top). Additionally in time-step six, the pattern of ETRANS transitions to a higher wave number, and BTEC (right column, contours) begins acting as a sink of energy, which continues into time-step seven. As the waves approach Argyre in time-step eight, the upstream wave weakens along with the BCEC and transport terms, but the downstream wave continues to have strong BCEC. As the downstream eddy crosses Argyre, it, too, drops in intensity, and by the final time-step, the waves dissipate. In time-step nine, a new eddy begins in the same area as before, with GFC on the eastern side of Hellas.

The baroclinic downstream development is made more transparent looking in the meridional direction (Fig. 13). The first eddy west of Hellas never extends into the basin and shrinks in vertical extent during transit. EKE (left column) and GFC (right column) show the classic westerly tilt of baroclinic waves. Upon reaching the eastern side, BCEC (right column, contours) begins, and simultaneously, the tilt of the associated EKE increases. Geopotential flux divergence transports EKE downstream to a region of GFC, where the second and third waves start to develop in time-step five. Negative BTEC on the upstream side of both of the waves in time-steps six and seven agrees with the traditional paradigm of barotropic transient wave decay (Orlanski and Sheldon, 1995), but there is a region of positive BTEC between the waves, showing that waves do gain some energy from the mean flow on their downstream edges.

4.3. Pause

Finally, in contrast to the two vigorous waves of the pre- and post-pause periods, one of the strongest waves from the pause period is shown from MY 25, $L_s = 96.83^\circ$ – 98.90° , which is representative of how waves interact with Tharsis and how BTEC contributes to wave growth during the pause period (Fig. 14) [labeled

C in Fig. 11]. Initially, there is an EKE center (left column) north of Hellas, as well as negative BCEC (middle column, contours) and a dipole of ETRANS (right column) in Hellas Planitia. At the second time-step, there is more organization in the GFC field (middle column), which becomes stronger in the third time-step. In the fourth time-step, BCEC is triggered just south and west of Tharsis, leading to strengthening of EKE. By time-step seven, eddy activity and BCEC is reduced, but EKE flares again in two places in time-step eight: one area directly over Tharsis and Solis Planum, with associated positive BCEC and BTEC (right column, contours), and an area west of Hellas, which has strong geopotential flux divergence, negative BCEC, but widespread positive BTEC, demonstrating the barotropic nature of these waves. EKE in the area west of Hellas dissipates in the following time-step, but large values of EKE remain in the Tharsis region. Though some aspects of the development of the pause wave are similar to the pre- and post-pause waves regarding the horizontal placement of EKE, the vertical distribution of pause storms is quite different (not shown). EKE is confined mostly above 300Pa. Unlike in the cases of the pre- and post-pause storms, BCEC is further aloft and has equally strong positive and negative regions. BTEC has negative and positive regions, with the latter compensating for the negative BCEC. GFC is also mostly confined to the upper-levels.

5. Discussion

Southern hemisphere transient waves have not been as thoroughly investigated as their northern hemisphere counterparts for a variety of reasons – mostly because southern hemisphere waves are weaker. However, southern hemisphere waves exhibit similar energetics to waves in the northern hemisphere.

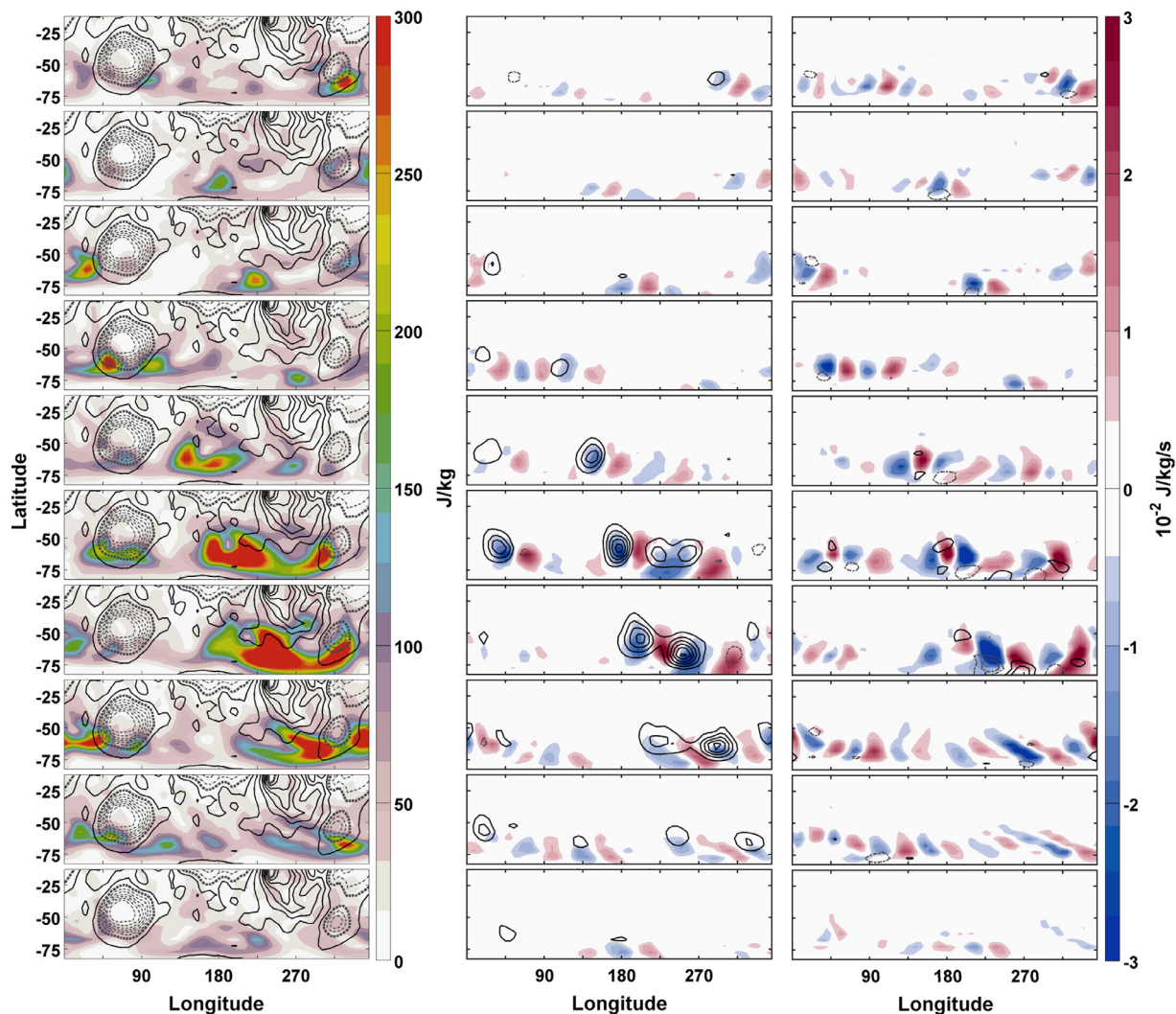


Fig. 12. As in Fig. 10 but for a wave development during the time period MY 24 $L_s = 166.31^\circ$ – 168.82° . The contour interval for BCEC and BTEC is 0.05 J/kg/s.

5.1. Time-mean energetics

The growth of waves is predicated on BCEC. In the southern hemisphere, waves grow in the flat highlands and decay upon interacting with the basins. BCEC and EKE are strongest in the 40°–75°S latitude band and between 30° and 60°E and 150° and 300°E. Though positive BCEC is preferred at different pressure levels during the pre- and post-pause seasons (Fig. 5), BCEC maxima are roughly the same height above the ground, as the surface pressure is lower during the post-pause season. Most non-pause waves have upper-level BCEC that is collocated with negative geopotential fluxes, and negative upper-level BCEC is collocated with GFC. Waves grow when the geopotential flux divergence and BCEC are collocated but decay when GFC is collocated with BCEC. An example can be seen in Fig. 13.

There are many more areas of negative time-averaged BCEC in the southern hemisphere than in the northern hemisphere (Fig. 5). Negative vertical heat flux on the eastern side of Hellas appears to be the main contributor to the negative BCEC, as the pattern is not present in the meridional heat fluxes (Fig. 6), but the negative meridional heat flux is the cause of the negative BCEC above 100 Pa in all periods, except the post-pause period in MY 24.

Waves are also found to grow by BTEC. This is in contrast to the development paradigm of Orlanski and Katzfey (1991), Swanson and Pierrehumbert (1994), and Mak (2000), whereby

barotropic decay is the primary mechanism by which wave packets are truncated in the upstream direction; however, terrestrial observations have indicated that this mechanism is not always unequivocal (McLay and Martin, 2002; Ahmadi-Givi et al., 2014). During the pause period, barotropic growth is found to dominate over baroclinic growth in the time average, which is counter to terrestrial studies that indicate that only individual waves tend to grow barotropically (Chang, 2000, 2001). The westerly jet is strongest during the pause period and waves feed off this jet energy through BTEC. However, some eddies, like that of the post-pause example in Section 4.2, decay by BTEC according to the energetics paradigm, and there are large areas of time-mean negative BTEC in the post-pause period. This indicates that the jet is not solely Hadley circulation driven like the subtropical jet on Earth nor solely eddy driven like the midlatitude jet on Earth. In this way, the westerly jet on Mars takes characteristics from both the terrestrial subtropical and midlatitudes jets on Earth and is similar to times in the terrestrial midwinter when the two jets merge (Lee and Kim, 2003).

5.2. Seasonal variability

Hollingsworth et al. (1997) was the first to find that in the southern hemisphere, the post-pause waves were the strongest – a finding that was confirmed in subsequent work (Wang and Richardson, 2015; Lewis et al., 2016). There is no consensus answer

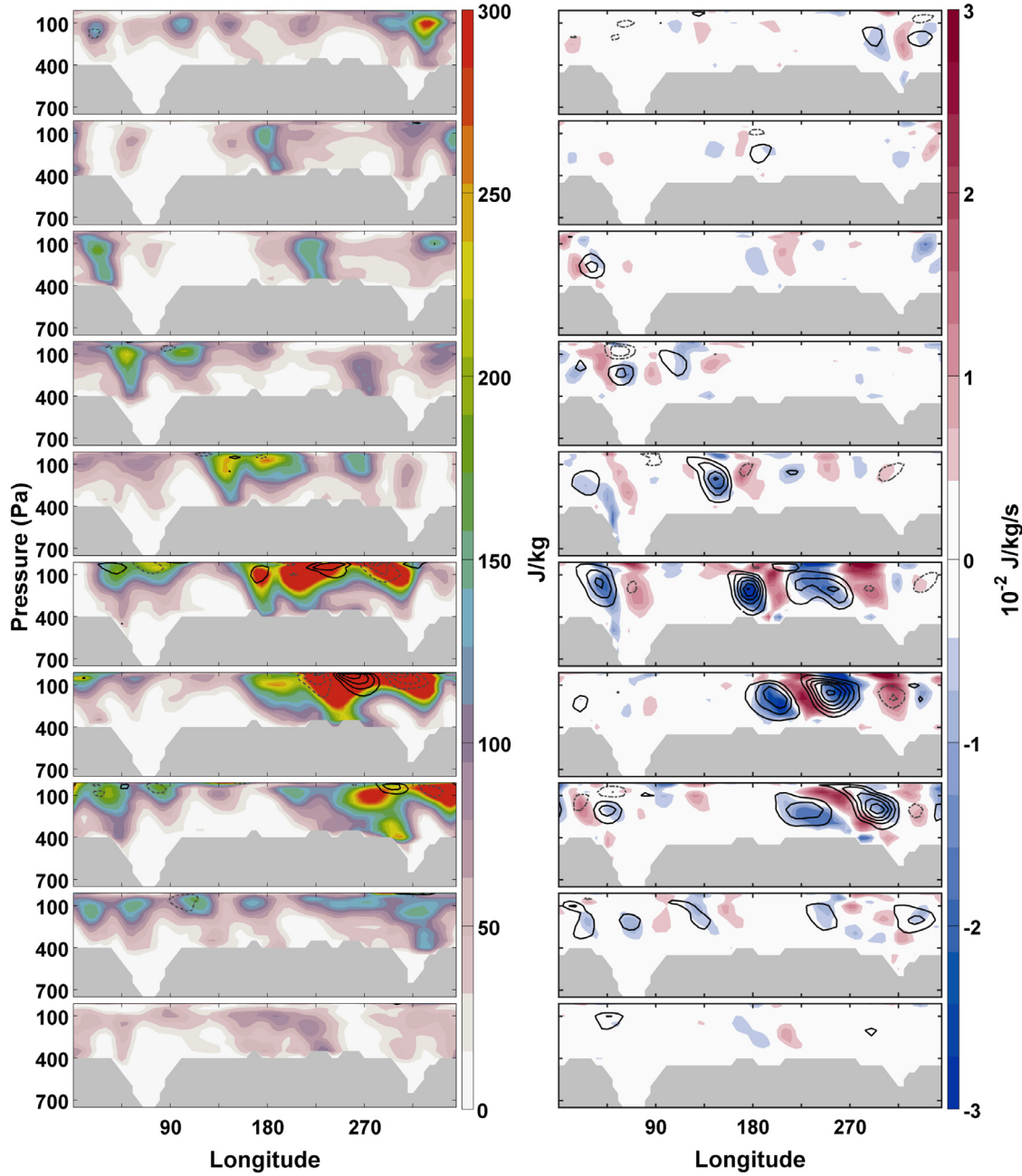


Fig. 13. The meridional average of the eddy diagnostics of the wave development depicted in Fig. 12. Shown are (left) EKE and BTEC (contours with 0.05 J/kg/s intervals) with negative values dashed and (right) GFC and BCEC (contours with 0.05 J/kg/s intervals) with negative values dashed.

for why this occurs; however, an investigation of the baroclinic parameter (Eady index) suggests a possible explanation. Fig. 15 shows the vertical profile of the averaged Eady index, vertical wind shear, and Brunt–Väisälä frequency between 57.5° and 82.5°S for each period. The Eady index (Hoskins and Valdes, 1990) quantifies the sensitivity of the flow to baroclinic instability and is defined as

$$\sigma = 0.31 f \left(\frac{\partial u}{\partial z} \right) (N)^{-1}, \tag{5}$$

where N is the Brunt–Väisälä frequency, f is the Coriolis parameter, and u is the zonal wind component. The vertical profile of the Eady index is highest in the post-pause period between 450 and 100 Pa, which is the most favored region for BCEC (Fig. 5). The Eady index in the pre-pause periods lies between the post-pause and pause periods. The reason for the increased Eady in-

dex in the post-pause period is due to decreased Brunt–Väisälä frequency above 350 Pa and increased vertical wind shear above 500 Pa. Below 350 Pa, the Brunt–Väisälä frequency is higher (indicating a more stable atmosphere) during the post-pause period, but the high stability is close to the surface and is offset by much higher vertical wind shear due to a westerly jet slightly closer to the surface. Each of these differences is related to the general circulation and time-mean average temperature. The meridional temperature gradient between 20° and 80°S is higher in the post-pause period compared to the pre-pause period (Fig. 1). Consequently, the westerly jet is also pushed closer to the pole. With the jet stream moved closer to pole, there is an area of warm air along the surface in the post-pause period extending through the middle latitudes. This is the cause of the high values of N below 350 Pa, but this area also increases the tilt of isotherms away from the

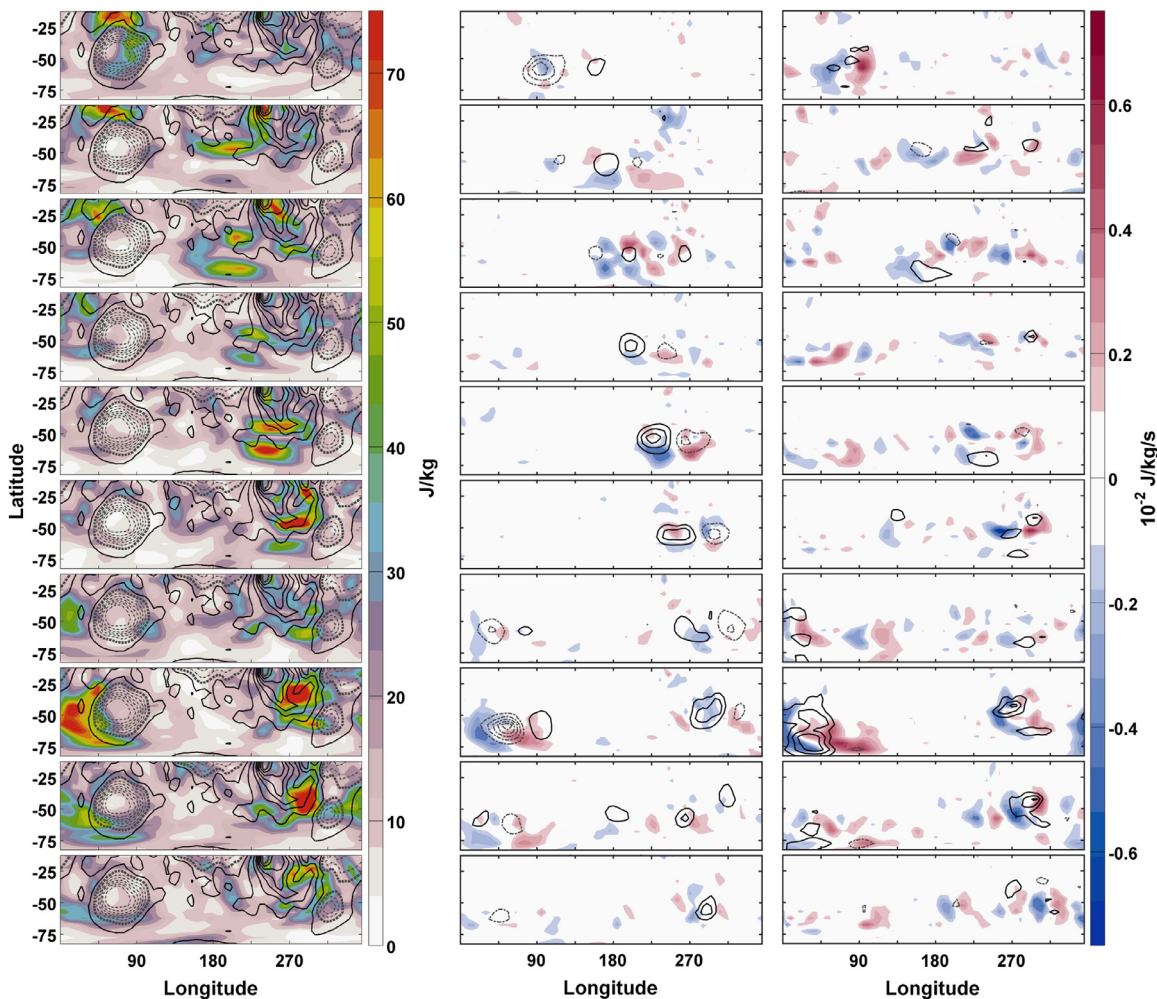


Fig. 14. As in Fig. 12 but for a wave development during the time period MY 25 $L_s = 96.83^\circ$ – 98.90° . The contour interval for BCEC and BTEC is 0.0075 J/kg/s.

pole above 300 Pa, enhancing the instability in the region of highest BCEC. This slight asymmetry in the position of the jet, the horizontal temperature gradient, and the vertical tilt of isotherms contributes to the stronger post-solstice period of eddies in the southern hemisphere.

The increased intensity of post-pause waves is also supported by AGF fluxes that serve to recirculate EKE from the downstream edge of the zonal storm track that ends at the southern tip of Tharsis back towards the upstream edge, east of Hellas. Recirculation also occurs in the shorter track between Argyre and Hellas. This is demonstrated by comparing the third rows of Figs. 2 and 4. At the downstream edge of the storm zone, AGF fluxes are directed north into a band of westward fluxes between 40° and 65° S. At the upstream edge, the fluxes are directed back to the south. In the pre-pause, AGF fluxes in the 40° to 65° S latitude band have a comparable magnitude to AGF fluxes in the post-pause period only on the western flank of Tharsis and are directed not towards the west but to the northwest, parallel to the pre-pause storm track. The fluxes in the post-pause period, excluding the post-pause MY 25 case, are also slightly stronger than the pre-pause fluxes. This recirculation of extant EKE reinforces the more zonal storm track and provides a stronger source for repeated baroclinic downstream development. A similar AGF recirculation process was noted terrestrially (Orlanski and Sheldon, 1995; Chang, 2000, 2001).

As a secondary consideration, the post-pause period may be intensified by the evaporation of the polar ice cap, which intensifies meridional temperature gradients. This is indirectly established in

the zonal average temperature in Fig. 1. Forget (1998) noted that the area of strongest sublimation later in spring is between 160° and 300° E in the southern hemisphere, which corresponds to the largest increase in the meridional heat flux in the post-pause period (Fig. 6 right column). The reduced magnitude of the southern hemisphere energetics allows for this effect to be observed, as opposed to the northern hemisphere, where the coherence and higher amplitude of the waves masks the contribution from diabatic effects.

5.3. Inter-annual variability

Inter-annual variability is important in the southern hemisphere. During the post-pause period, EKE is high in MY 24 and 25. The energetics of MY 25 is strong due to the diabatically forced dust-lifting centers during the GDS. The strong energetics of MY 24 is due to the high coherence and periodicity of waves during this period (Fig. 11). These strong waves in MY 24 were noted by Hinson and Wilson (2002) as 2-sol period, wave number 3 waves from TES limb retrievals.

A time series of the EKE equation terms is shown in Fig. 16. The largest EKE and BCEC in the pre-pause period – both in a background average value and in the intensity of EKE peaks – is found in MY 25. The strength of the MY 25 pre-pause energetics could be a result of the weak “C” dust event in MY 24 (Kass et al., 2016). Similarly, the reduced EKE of MY 27 could possibly result from the intense “C” storm in MY 26 that served to increase high-level haze

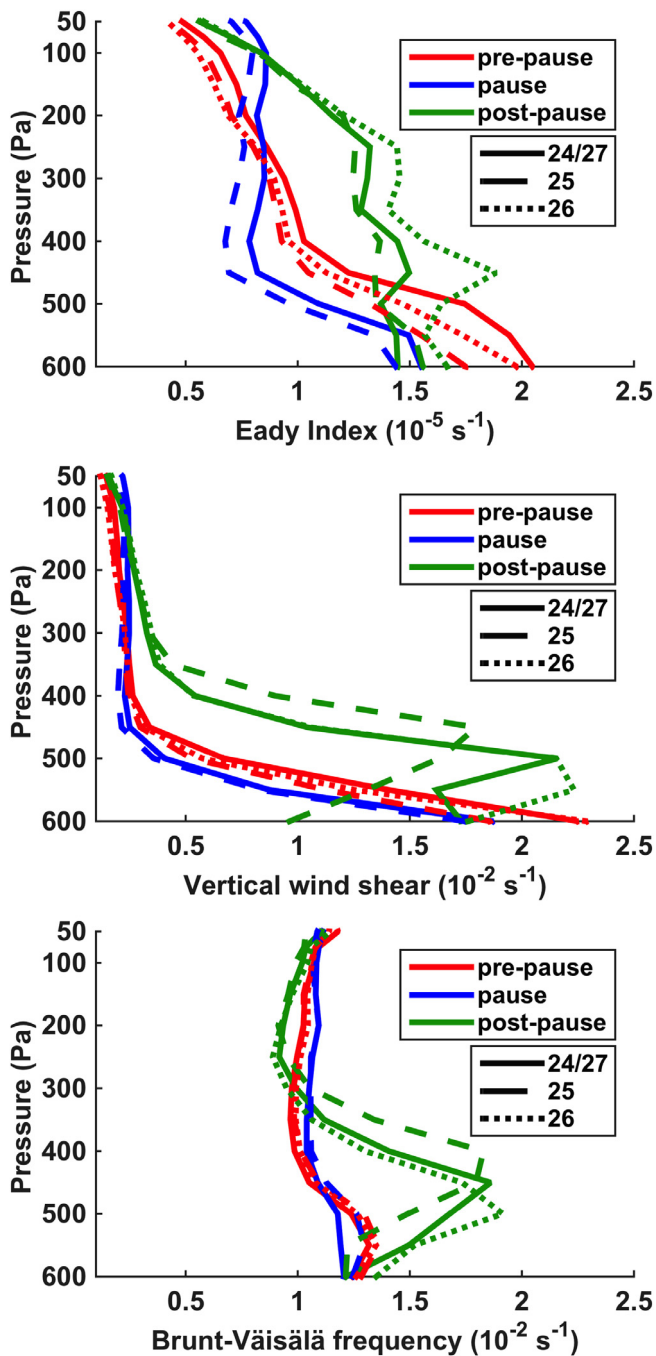


Fig. 15. The vertical profile of the Eady index (top), vertical wind shear (middle), and Brunt-Väisälä frequency (bottom) for each period averaged in the 57.5°–82.5°S latitude band.

and reduce baroclinicity. ETRANS, GFC, and BTEC are all comparable in intensity between each year. Both MY 25 and 26 transition to the pause-period level of activity around the same time ($L_s = 60^\circ$). The pause period has little variability, with minor exceptions, but wave activity resumes at a higher level approximately $L_s = 20^\circ$ sooner in MY 26 than in MY 25.

After $L_s = 150^\circ$, two inter-annual effects are important. The EKE activity rapidly increases and has the strongest average in MY 25, with the exception of one wave during MY 24. Stronger, longer-duration EKE activity in the post-pause period in MY 25 is due to the GDS. Unfortunately, the MACDA GCM ran freely during a long portion of the GDS intensification period ($\sim L_s = 152^\circ$ – 164°) but

was able to capture the time immediately preceding the intensification and the time directly afterwards, and both EKE and BCEC are higher in these periods. Interestingly, BTEC during the GDS is not substantively increased above that of other years. Secondly, EKE and BCEC during MY 26 are less than that found in either MY 24 or 25 during the post-pause period. This is not due to natural inter-annual variability but to the reduction in heat fluxes as a result of errors in the TES temperature profile in the lowest few scale heights around the south pole (Pankine, 2015, 2016). Regardless, the intensity of all EKE equation terms is considerably larger in the post-pause period compared to the pre-pause period.

Throughout the transient wave period between $L_s = 10^\circ$ – 180° , the bottom two scale heights contain eastward moving waves, but in MY 25, the waves abruptly switch direction and travel westward after $L_s = 185^\circ$, within a much longer period easterly wave packet (greater than 20 sols) (not shown). These waves are confined above 10Pa and could be westerly traveling Rossby waves. If so, they should be barotropic in nature, as there was little BCEC noted with the activity. It is equally possible, since the phenomena only occurs at the top vertical levels, that this feature is an artifact of MACDA itself. However, this type of wave is similar to the “slow” easterly wave found in GFDL MGCM simulations (Wilson et al., 2002). This wave had a weak near-surface response and was possibly caused by an inertial instability from an oscillating meridional overturning circulation with strong barotropic energy conversion. Furthermore, middle atmosphere westward waves are noted to coincide with major dust storm events, like the GDS (Wang, 2017), and high altitude dust during the GDS was observed to follow a westward wave number 1 pattern (Clancy et al., 2010). Waves at these heights have been shown to be dominated by a wave number 1 structure (Banfield et al., 2004), emerging from barotropic sources (Wang and Toigo, 2016). This also explains why BCEC becomes slightly negative during the pause as well as why the upper-level waves are shown to be lacking in baroclinicity in the northern hemisphere (Wang and Toigo, 2016). The high altitude of these pause waves is also the cause of the downward directed AGF fluxes seen in the southern hemisphere, as energy is directed from the upper-levels towards the surface (Fig. 8).

It should be noted that the waves investigated here are not directly related to the lifting of dust during the classical dust season on Mars, lasting between $L_s = 200^\circ$ – 330° . These regional dust events are attributed to flushing activity from transient eddies from the northern hemisphere (Kass et al., 2016). The southern hemisphere transient eddies are found to be substantially weaker than their northern counterparts, and individual southern hemisphere eddies cannot easily lift the mass necessary to trigger regional dust storms.

5.4. Hemispheric variability

The time-mean energetics of southern hemisphere waves is weaker than that of the northern hemisphere but is otherwise similar. Individual waves share many characteristics to northern hemisphere waves but also have energetics that are half the amplitude of northern hemisphere waves. Eddies from the MY 24 post-pause period and the long-period, large wave number eddies from the MY 27 pre-pause period show that despite the slower and zonally shorter character of some southern hemisphere waves, eddies grow baroclinically and decay mostly through friction.

The paths of individual eddies are zonally more localized in the southern than in the northern hemisphere. This is particularly true during the pre-pause period (Fig. 11), where eddy amplitudes are maximized between 180° and 300° E and lose their coherence crossing Hellas. Eddies in the post-pause period are more like those in the northern hemisphere that circumnavigate the planet multiple times, though eddies do decrease in amplitude

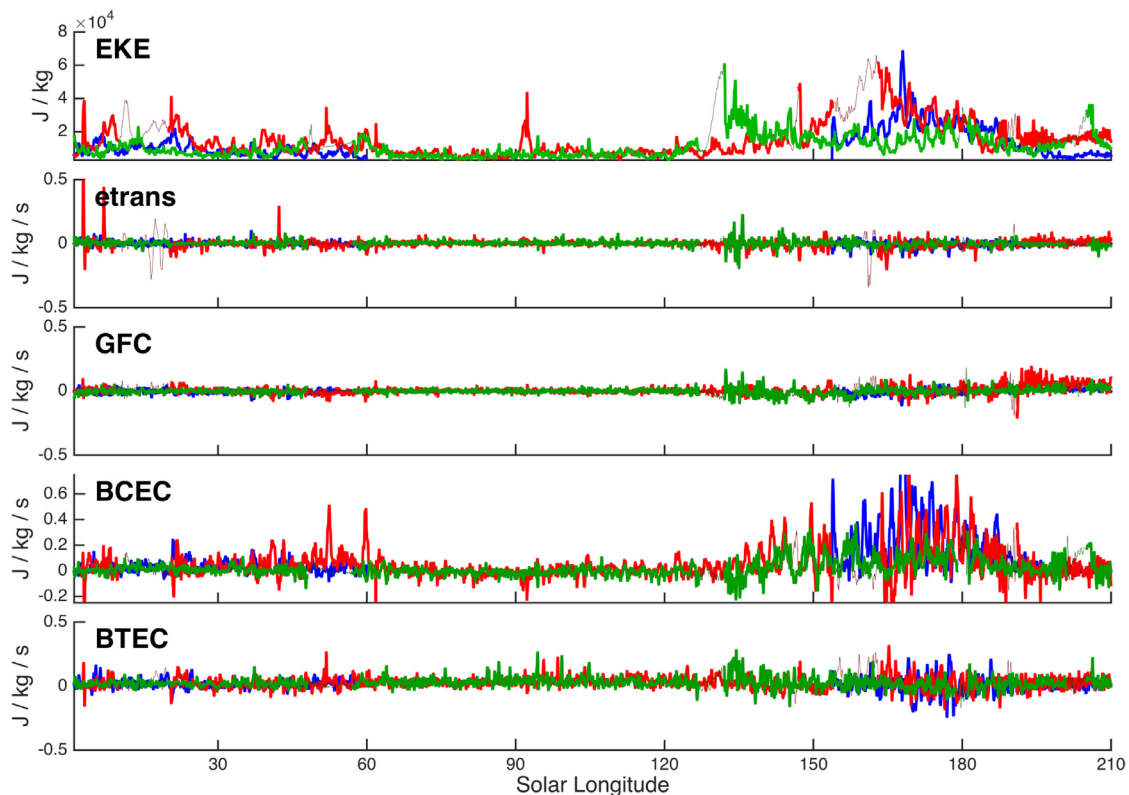


Fig. 16. Summed, pressure-weighted EKE equation terms in the 57.5°–82.5° S band for MY 27 ($L_s = 20^\circ$ – 60°) and MY 24 ($L_s = 153.7^\circ$ – 180°) in blue, MY 25 in red, and MY 26 in green. Times longer in duration than $L_s = 1^\circ$ when TES retrievals were unavailable and the MACDA GCM ran freely are indicated by thin lines. (For interpretation of the references to color in this figure legend, the reader is referred to the web version of this article.)

while crossing Hellas. Observations have borne this out, as frontal dust storms are more separated and are shorter in duration in the southern hemisphere (Wang and Richardson, 2015). The topography of the southern hemisphere could cause stationary waves to modulate the amplitudes of the eddies, leading to a localization of wave activity and the zonal extent of the storm track (Chang and Orlanski, 1993). The case of the post-pause wave development provides an example of this phenomenon (Fig. 12). Eddies generally shrink in vertical extent when they move across the large basins. A shallow layer of GFC near the surface in the basins and AGF fluxes directed towards the surface (Fig. 8) transport EKE to where friction can reduce the strength of the eddies. Additionally, AGF fluxes are directed back to the west on the upstream side of Tharsis, which recirculates EKE. However, the storm tracks in the post-pause period are more zonal than in the pre-pause period, which has a predominant northwest to southeast track across Terra Cimmeria and Terra Sirenum. This is due to the more zonal transport by ETRANS in the post-pause periods (Fig. 4).

The zonally asymmetric terrain (e.g., Blumsack and Gierasch, 1972; Hollingsworth and Barnes, 1996) and the associated topographically forced stationary waves (Mulholland et al., 2016) have been repeatedly cited as the reason for the weaker southern hemisphere wave activity, but a second explanation is also plausibly indicated by the energetics results: a shortened vertical atmospheric column. The vertical stability profile does not change substantially above 10 Pa between the southern and northern hemispheres (Fig. 1 compared to B16 Fig. 2), but the terrain is much higher on average in the southern hemisphere. Temperatures increase with height above 10 Pa in the northern and southern hemispheres, limiting baroclinic instability, but the zonal mean topography in the northern hemisphere is roughly 100 to 200 Pa lower than in the southern hemisphere. The lowest BCEC occurs at roughly the

same height above the surface in both hemispheres – 700 Pa in the northern hemisphere and 500 Pa in the southern hemisphere, but the top of the BCEC maximum is capped at around 100 Pa in both hemispheres (compare Fig. 5 to B16 Fig. 7). Furthermore, the meridional and zonal heat fluxes are vertically compressed in the same way in the southern hemisphere (Fig. 6), and the Eady index in the northern hemisphere is highest between 700 and 800 Pa (B16 Fig. 10), which is a feature that occurs between 500 and 600 Pa in the southern hemisphere (Fig. 15). The reduced vertical column thus limits the amount of unstable vertical profile that can undergo baroclinic conversion. The post-pause case study (Fig. 13) corroborates this hypothesis. In time steps 5–8, BCEC only occurs between 400 Pa (the surface) and 100 Pa. This is compared to the case studies in B16, namely B16 Fig. 15, where BCEC is maximized between 400 and 100 Pa but also continues to the surface at 700 Pa, providing additional BCEC to generate EKE. Confirming this diagnostic result with modeling studies will be the subject of future research.

6. Conclusions

The energetics of transient waves of the southern hemisphere of Mars was investigated using the MACDA reanalysis. The eddy kinetic energy equation was investigated for four time periods – summer and winter solstice, a late fall period, and an early spring period.

Individual wave packets in the southern hemisphere are similar to their northern hemisphere counterparts as found in Battalio et al. (2016) but are less intense. Waves are initiated by geopotential flux convergence, driven by baroclinic and barotropic energy conversion, and decay through a combination of barotropic energy conversion, geopotential flux divergence, and

friction. Waves intermittently extract energy from the mean flow, suggesting that the westerly jet shares characteristics between a subtropical – angular momentum conserving – jet and an eddy-driven jet. A shorter atmospheric column in the southern hemisphere might contribute to the depressed energetics of the southern hemisphere waves by reducing the vertical distance over which the atmosphere is baroclinically unstable, complementing the conclusion of Mulholland et al. (2016) that southern hemisphere eddies are weaker due to the more zonally asymmetric topography.

Waves in the southern hemisphere are stronger after the winter solstitial pause due to a more favorable general circulation and temperature profile in the post-pause period that increases the vertical and meridional temperature gradients and by ageostrophic geopotential fluxes that recirculate EKE from the end of the storm track back to the front. The strengthening of the meridional temperature gradient is possibly due to the sublimation of the CO₂ ice cap in the post-pause period. Topography prevents zonal propagation of the transient waves in the fall, which instead travel from the northwest of Hellas Planitia towards the southeast and ending at the southern tip of Tharsis. A second, shorter wave track exists between Argyre and Hellas Planitia. During the spring season, waves have a more zonal track thanks to stronger zonal eddy kinetic energy fluxes. Transient, baroclinic waves are nonexistent during the summer, and during the winter, there is a reduction in wave activity due to the tilt of the polar front.

Future work includes the expansion of energetics analysis to the entirety of the northern hemisphere wave activity, spectral decomposition of the waves to ascertain differences in the energetics of waves of different wave number, investigation of the relationship between the westerly jet and traveling waves, modeling studies to ascertain the difference in strength between pre-pause and post-pause energetics, and comparison of new reanalysis datasets to MACDA.

Acknowledgments

The helpful comments of John Wilson and an anonymous reviewer improved the results. This work fulfills part of the Ph.D. requirements of the first author.

Supplementary material

Supplementary material associated with this article can be found, in the online version, at doi: [10.1016/j.icarus.2018.03.015](https://doi.org/10.1016/j.icarus.2018.03.015).

References

- Ahmadi-Givi, F., Nasr-Esfahany, M., Mohebalhojeh, A.R., 2014. Interaction of north atlantic baroclinic wave packets and the mediterranean storm track. *Q. J. R. Meteorol. Soc.* 140, 754–765. doi:[10.1002/qj.2171](https://doi.org/10.1002/qj.2171).
- Banfield, D., Conrath, B., Gierasch, P., Wilson, R., Smith, M., 2004. Traveling waves in the martian atmosphere from MGS TES nadir data. *Icarus* 170, 365–403. doi:[10.1016/j.icarus.2004.03.015](https://doi.org/10.1016/j.icarus.2004.03.015).
- Barnes, J.R., 1980. Time spectral analysis of midlatitude disturbances in the Martian atmosphere. *J. Atmos. Sci.* 37, 2002–2015.
- Barnes, J.R., 1981. Midlatitude disturbances in the martian atmosphere: a second Mars year. *J. Atmos. Sci.* 38, 225–234.
- Barnes, J.R., Pollack, J.B., Haberle, R.M., Leovy, C.B., Zurek, R.W., Lee, H., Schaeffer, J., 1993. Mars atmospheric dynamics as simulated by the NASA ames general circulation model 2. transient baroclinic eddies. *J. Geophys. Res.* 98, 3125–3148.
- Basu, S., Wilson, J., Richardson, M., Ingersoll, A., 2006. Simulation of spontaneous and variable global dust storms with the GFDL Mars GCM. *J. Geophys. Res.* 111, E09004. doi:[10.1029/2005JE002660](https://doi.org/10.1029/2005JE002660).
- Battalio, M., Dyer, J., 2017. The minimum length scale for evaluating QG omega using high-resolution model data. *Mon. Weather Rev.* 145, 1659–1678. doi:[10.1175/MWR-D-16-0241.1](https://doi.org/10.1175/MWR-D-16-0241.1).
- Battalio, M., Szunyogh, I., Lemmon, M., 2016. Energetics of the martian atmosphere using the Mars analysis correction data assimilation (MACDA) dataset. *Icarus* 276, 1–20. doi:[10.1016/j.icarus.2016.04.028](https://doi.org/10.1016/j.icarus.2016.04.028).
- Battalio, M., Szunyogh, I., Lemmon, M., 2018. Corrigendum to “energetics of the martian atmosphere using the Mars analysis correction data assimilation (MACDA) dataset”. *Icarus* 203, 565–567. [*icarus* 276 (2016) 1–20].
- Blumsack, S.L., Gierasch, P.J., 1972. Mars: the effects of topography on baroclinic instability. *J. Atmos. Sci.* 29, 1081–1089.
- Chang, E.K.M., 1993. Downstream development of baroclinic waves as inferred from regression analysis. *J. Atmos. Sci.* 50, 2038–2053.
- Chang, E.K.M., 2000. Wave packets and life cycles of troughs in the upper troposphere: examples from the southern hemisphere summer season of 1984/85. *Mon. Weather Rev.* 128, 25–50. doi:[10.1175/1520-0493\(2000\)128\(0025:WPALCO\)2.0.CO;2](https://doi.org/10.1175/1520-0493(2000)128(0025:WPALCO)2.0.CO;2).
- Chang, E.K.M., 2001. The structure of baroclinic wave packets. *J. Atmos. Sci.* 58, 1694–1713. doi:[10.1175/1520-0469\(2001\)058\(1694:TSOBWP\)2.0.CO;2](https://doi.org/10.1175/1520-0469(2001)058(1694:TSOBWP)2.0.CO;2).
- Chang, E.K.M., Lee, S., Swanson, K.L., 2002. Storm track dynamics. *J. Clim.* 15, 2163–2183.
- Chang, E.K.M., Orlanski, I., 1993. On the dynamics of storm track. *J. Atmos. Sci.* 50, 999–1015.
- Clancy, R.T., Wolff, M.J., Whitney, B.A., Cantor, B.A., Smith, M.D., McConnochie, T.H., 2010. Extension of atmospheric dust loading to high altitudes during the 2001 Mars dust storm: MGS TES limb observations. *Icarus* 207, 98–109. doi:[10.1016/j.icarus.2009.10.011](https://doi.org/10.1016/j.icarus.2009.10.011).
- Decker, S.G., Martin, J.E., 2005. A local energetics analysis of the life cycle differences between consecutive, explosively deepening, continental cyclones. *Mon. Weather Rev.* 133, 295–316.
- Forget, F., 1998. Mars CO₂ Ice Polar Caps. In: *Solar System Ices*. Springer, pp. 477–507.
- Forget, F., Hourdin, F., Fournier, R., Hourdin, C., Talagrand, O., Collins, M., Lewis, S.R., Read, P.L., Huot, J.P., 1999. Improved general circulation models of the martian atmosphere from the surface to above 80 km. *J. Geophys. Res.* 104, 24155. doi:[10.1029/1999JE001025](https://doi.org/10.1029/1999JE001025).
- Greybush, S.J., Kalnay, E., Hoffman, M.J., Wilson, R.J., 2013. Identifying martian atmospheric instabilities and their physical origins using bred vectors. *Q. J. R. Meteorol. Soc.* 139, 639–653. doi:[10.1002/qj.1990](https://doi.org/10.1002/qj.1990).
- Guzewich, S.D., Toigo, A.D., Kulowski, L., Wang, H., 2015. Mars orbiter camera climatology of textured dust storms. *Icarus* 258, 1–13. doi:[10.1016/j.icarus.2015.06.023](https://doi.org/10.1016/j.icarus.2015.06.023). <http://linkinghub.elsevier.com/retrieve/pii/S0019103515002675>.
- Guzewich, S.D., Toigo, A.D., Wang, H., 2017. An investigation of dust storms observed with the Mars color imager. *Icarus* 289, 199–213. doi:[10.1016/j.icarus.2017.02.020](https://doi.org/10.1016/j.icarus.2017.02.020). <http://linkinghub.elsevier.com/retrieve/pii/S001910351630690X>.
- Ha, Y., Zhong, Z., Zhu, Y., Hu, Y., 2013. Contributions of barotropic energy conversion to the northwest pacific tropical cyclone during ENSO. *Mon. Weather Rev.* 141, 1337–1346. doi:[10.1175/MWR-D-12-00084.1](https://doi.org/10.1175/MWR-D-12-00084.1). <http://journals.ametsoc.org/doi/abs/10.1175/MWR-D-12-00084.1>.
- Hayne, P.O., Paige, D.A., Heavens, N.G., 2014. The role of snowfall in forming the seasonal ice caps of Mars: models and constraints from the Mars climate sounder. *Icarus* 231, 122–130. doi:[10.1016/j.icarus.2013.10.020](https://doi.org/10.1016/j.icarus.2013.10.020).
- Hayne, P.O., Paige, D.A., Schofield, J.T., Kass, D.M., Kleinböhl, A., Heavens, N.G., McCleese, D.J., 2012. Carbon dioxide snow clouds on Mars: south polar winter observations by the Mars climate sounder. *J. Geophys. Res. E: Planets* 117, 1–23. doi:[10.1029/2011JE004040](https://doi.org/10.1029/2011JE004040).
- Hinson, D.P., Wilson, R.J., 2002. Transient eddies in the southern hemisphere of Mars. *Geophys. Res. Lett.* 29, 3–6. doi:[10.1029/2001GL014103](https://doi.org/10.1029/2001GL014103).
- Hollingsworth, J.L., Barnes, J.R., 1996. Forced stationary planetary waves in Mars's winter atmosphere. *J. Atmos. Sci.* 53, 428–448.
- Hollingsworth, J.L., Haberle, R.M., Schaeffer, J., 1997. Seasonal variations of storm zones on Mars. *Adv. Space Res.* 19, 1237–1240. doi:[10.1016/S0273-1177\(97\)00275-5](https://doi.org/10.1016/S0273-1177(97)00275-5).
- Hoskins, B.J., Valdes, P.J., 1990. On the existence of storm-tracks. *J. Atmos. Sci.* 47, 1854–1864.
- Imamura, T., Kobayashi, H., 2009. Wavenumber spectra of planetary-scale disturbances in the Mars atmosphere. *Icarus* 199, 286–294. doi:[10.1016/j.icarus.2008.09.021](https://doi.org/10.1016/j.icarus.2008.09.021).
- Jiang, T., Deng, Y., Li, W., 2013. Local kinetic energy budget of high-frequency and intermediate-frequency eddies: winter climatology and interannual variability. *Clim. Dyn.* 41, 961–976. doi:[10.1007/s00382-013-1684-1](https://doi.org/10.1007/s00382-013-1684-1).
- Kass, D.M., Kleinböhl, A., McCleese, D.J., Schofield, J.T., Smith, M.D., 2016. Interannual similarity in the Martian atmosphere during the dust storm season. *Geophys. Res. Lett.* 43. doi:[10.1002/2016GL068978](https://doi.org/10.1002/2016GL068978).
- Kavulich, M.J., Szunyogh, I., Gyarmati, G., Wilson, R.J., 2013. Local dynamics of baroclinic waves in the martian atmosphere. *J. Atmos. Sci.* 70, 3415–3447. doi:[10.1175/JAS-D-12-0262.1](https://doi.org/10.1175/JAS-D-12-0262.1).
- Kuroda, T., Medvedev, A.S., Hartogh, P., Takahashi, M., 2007. Seasonal changes of the baroclinic wave activity in the northern hemisphere of Mars simulated with a GCM. *Geophys. Res. Lett.* 34, L09203. doi:[10.1029/2006GL028816](https://doi.org/10.1029/2006GL028816).
- Kuroda, T., Medvedev, A.S., Kasaba, Y., Hartogh, P., 2013. Carbon dioxide ice clouds, snowfalls, and baroclinic waves in the northern winter polar atmosphere of Mars. *Geophys. Res. Lett.* 40, 1484–1488. doi:[10.1002/grl.50326](https://doi.org/10.1002/grl.50326).
- Lee, S., Kim, H.K., 2003. The dynamical relationship between subtropical and eddy-driven jets. *J. Atmos. Sci.* 60, 1490–1503.
- Leovy, C.B., 1969. Mars: theoretical aspects of meteorology. *Appl. Opt.* 8, 1279–1286.
- Lewis, S.R., Mulholland, D.P., Read, P.L., Montabone, L., Wilson, R.J., Smith, M.D., 2016. The solstitial pause on Mars: 1. a planetary wave reanalysis. *Icarus* 264, 456–464. doi:[10.1016/j.icarus.2015.08.039](https://doi.org/10.1016/j.icarus.2015.08.039).
- Lewis, S.R., Read, P.L., Conrath, B.J., Pearl, J.C., Smith, M.D., 2007. Assimilation of thermal emission spectrometer atmospheric data during the Mars global surveyor aerobraking period. *Icarus* 192, 327–347. doi:[10.1016/j.icarus.2007.08.009](https://doi.org/10.1016/j.icarus.2007.08.009).
- Mak, M., 2000. Does an unstable baroclinic wave equilibrate/decay baroclinically or barotropically? *J. Atmos. Sci.* 57, 453–463. doi:[10.1175/1520-0469\(2000\)057\(0453:DAUBWE\)2.0.CO;2](https://doi.org/10.1175/1520-0469(2000)057(0453:DAUBWE)2.0.CO;2).

- McLay, J.G., Martin, J.E., 2002. Surface cyclolysis in the north pacific ocean. part III: composite local energetics of tropospheric-deep cyclone decay associated with rapid surface cyclolysis. *Mon. Weather Rev.* 130, 2507–2529. doi:[10.1175/1520-0493\(2002\)130\(2507:SCITNP\)2.0.CO;2](https://doi.org/10.1175/1520-0493(2002)130(2507:SCITNP)2.0.CO;2).
- Montabone, L., Marsh, K., Lewis, S.R., Read, P.L., Smith, M.D., Holmes, J., Spiga, A., Lowe, D., Pamment, A., 2014. The Mars analysis correction data assimilation (MACDA) dataset v1.0. *Geosci. Data J.* 1, 129–139. doi:[10.1002/gdj3.13](https://doi.org/10.1002/gdj3.13).
- Mooring, T.A., Wilson, R.J., 2015. Transient eddies in the MACDA Mars reanalysis. *J. Geophys. Res.: Planets* 120, 1–26. doi:[10.1002/2015JE004824](https://doi.org/10.1002/2015JE004824).
- Mulholland, D.P., Lewis, S.R., Read, P.L., Madeleine, J.B., Forget, F., 2016. The solsticial pause on Mars: 2 modelling and investigation of causes. *Icarus* 264, 465–477. doi:[10.1016/j.icarus.2015.08.038](https://doi.org/10.1016/j.icarus.2015.08.038).
- Noguchi, K., Morii, Y., Oda, N., Kuroda, T., Tellmann, S., Patzold, M., 2017. Role of stationary and transient waves in CO₂ supersaturation during northern winter in the Martian atmosphere revealed by MGS radio occultation measurements. *J. Geophys. Res.: Planets* 122, 1–15. doi:[10.1002/2016JE005142](https://doi.org/10.1002/2016JE005142).
- Orlanski, I., Chang, E.K.M., 1993. Ageostrophic geopotential fluxes in downstream and upstream development of baroclinic waves. *J. Atmos. Sci.* 50, 212–225.
- Orlanski, I., Katzfey, J., 1991. The life cycle of a cyclone wave in the southern hemisphere. part I: eddy energy budget. *J. Atmos. Sci.* 48, 1973–1998.
- Orlanski, I., Sheldon, J.P., 1993. A case of downstream baroclinic development over western North America. *Mon. Weather Rev.* 121, 2929–2950.
- Orlanski, I., Sheldon, J.P., 1995. Stages in the energetics of baroclinic systems. *Tellus* 47A, 605–628.
- Pankine, A.A., 2015. The nature of the systematic radiometric error in the MGS TES spectra. *Planet. Space Sci.* 109–110, 64–75. doi:[10.1016/j.pss.2015.01.022](https://doi.org/10.1016/j.pss.2015.01.022). <http://linkinghub.elsevier.com/retrieve/pii/S0032063315000379>.
- Pankine, A.A., 2016. Radiometric error and re-calibration of the MGS TES spectra. *Planet. Space Sci.* 134, 112–121. doi:[10.1016/j.pss.2016.10.015](https://doi.org/10.1016/j.pss.2016.10.015).
- Read, P.L., Lewis, S.R., Mulholland, D.P., 2015. The physics of martian weather and climate: a review. *Prog. Phys.* 78, 125901. doi:[10.1088/0034-4885/78/12/a=125901](https://doi.org/10.1088/0034-4885/78/12/a=125901). <http://stacks.iop.org/0034-4885/78/i=12/a=125901?key=crossref.d96a056962ed3903e3f32aa588a08068>.
- Seiki, A., Takayabu, Y.N., 2007. Westerly wind bursts and their relationship with intraseasonal variations and ENSO. part II: energetics over the western and central pacific. *Mon. Weather Rev.* 135, 3346–3361. doi:[10.1175/MWR3503.1](https://doi.org/10.1175/MWR3503.1).
- Smith, M.D., 2004. Interannual variability in TES atmospheric observations of Mars during 1999–2003. *Icarus* 167, 148–165. doi:[10.1016/j.icarus.2003.09.010](https://doi.org/10.1016/j.icarus.2003.09.010).
- Strausberg, M.J., 2005. Observations of the initiation and evolution of the 2001 Mars global dust storm. *J. Geophys. Res.* 110, E02006. doi:[10.1029/2004JE002361](https://doi.org/10.1029/2004JE002361).
- Swanson, K., Pierrehumbert, R.T., 1994. Nonlinear wave packet evolution on a baroclinically unstable jet. *J. Atmos. Sci.* 51, 384–396.
- Toigo, A.D., Waugh, D.W., Guzewich, S.D., 2017. What causes Mars' annular polar vortices? *Geophys. Res. Lett.* 44, 71–78. doi:[10.1002/2016GL071857](https://doi.org/10.1002/2016GL071857).
- Tsou, C.H., Hsu, H.H., Hsu, P.C., 2014. The role of multiscale interaction in synoptic-scale eddy kinetic energy over the western north pacific in autumn. *J. Clim.* 27, 3750–3766. doi:[10.1175/JCLI-D-13-00380.1](https://doi.org/10.1175/JCLI-D-13-00380.1).
- Wang, H., 2017. Major dust storms and westward traveling waves on Mars. *Geophys. Res. Lett.* 44, 3493–3501. doi:[10.1002/2017GL072894](https://doi.org/10.1002/2017GL072894).
- Wang, H., Richardson, M.I., 2015. The origin, evolution, and trajectory of large dust storms on Mars during Mars years 24–30 (1999–2011). *Icarus* 251, 112–127. doi:[10.1016/j.icarus.2013.10.033](https://doi.org/10.1016/j.icarus.2013.10.033).
- Wang, H., Richardson, M.I., Toigo, A.D., Newman, C.E., 2013. Zonal wavenumber three traveling waves in the northern hemisphere of Mars simulated with a general circulation model. *Icarus* 223, 654–676. doi:[10.1016/j.icarus.2013.01.004](https://doi.org/10.1016/j.icarus.2013.01.004).
- Wang, H., Richardson, M.I., Wilson, R.J., Ingersoll, A.P., Toigo, A.D., Zurek, R.W., 2003. Cyclones, tides, and the origin of a cross-equatorial dust storm on Mars. *Geophys. Res. Lett.* 30, 1488. doi:[10.1029/2002GL016828](https://doi.org/10.1029/2002GL016828).
- Wang, H., Toigo, A.D., 2016. The variability, structure and energy conversion of the northern hemisphere traveling waves simulated in a Mars general circulation model. *Icarus* 271, 207–221. doi:[10.1016/j.icarus.2016.02.005](https://doi.org/10.1016/j.icarus.2016.02.005).
- Wang, H., Toigo, A.D., Richardson, M.I., 2011. Curvilinear features in the southern hemisphere observed by Mars global surveyor Mars orbiter camera. *Icarus* 215, 242–252. doi:[10.1016/j.icarus.2011.06.029](https://doi.org/10.1016/j.icarus.2011.06.029).
- Waugh, D.W., Toigo, A.D., Guzewich, S.D., Greybush, S.J., Wilson, R.J., Montabone, L., 2016. Martian polar vortices: comparison of reanalyses. *J. Geophys. Res.: Planets* 121, 1–16. doi:[10.1002/2016JE005093](https://doi.org/10.1002/2016JE005093).
- Wilson, R.J., Banfield, D., Conrath, B.J., Smith, M.D., 2002. Traveling waves in the northern hemisphere of Mars. *Geophys. Res. Lett.* 29, 3–6. doi:[10.1029/2002GL014866](https://doi.org/10.1029/2002GL014866).
- Zhan, R., Wang, Y., Lei, X., 2011. Contributions of ENSO and east indian ocean SSTA to the interannual variability of northwest pacific tropical cyclone frequency. *J. Clim.* 24, 509–521. doi:[10.1175/2010JCLI3808.1](https://doi.org/10.1175/2010JCLI3808.1).